# Pattern identification of biomedical images with time series: contrasting THz pulse imaging with DCE-MRIs

Article

Accepted Version

It is advisable to refer to the publisher's version if you intend to cite from the work. See Guidance on citing.
Published version at: http://dx.doi.org/10.1016/j.artmed.2016.01.005
To link to this article DOI: http://dx.doi.org/10.1016/j.artmed.2016.01.005

# CentAUR

Central Archive at the University of Reading

Reading's research outputs online

# Pattern identification of biomedical images with time series: Contrasting THz pulse imaging with DCE-MRIs

X.-X. Yin [a], S. Hadjiloucas [b] Y. Zhang [a] J. Cao [c] Y. Miao [d] and D. Abbott [e]

[a] *Centre for Applied Informatics, College of Engineering and Science, Victoria University, Melbourne , VIC 8001, Australia*
[b] *School of Systems Engineering, University of Reading, Reading RG6 6AY, U.K.*
[c] *Nanjing University of Finance and Econimicsčňschool of Computer Science*
[d] *College of Engineering and Science, Victoria University, Melbourne, VIC 8001, Australia*
[e] *Centre for Biomedical Engineering (CBME) and School of Electrical & Electronic Engineering, The University of Adelaide, South Australia, Australia*

## Abstract

We provide a survey of recent advances in biomedical image analysis and classification from emergent imaging modalities such as terahertz (THz) pulse imaging (TPI) and dynamic contrast-enhanced magnetic resonance imaging (DCE-MRI) and identify their underlining commonalities. Both time and frequency domain signal pre-processing techniques are considered: noise removal, spectral analysis, principal component analysis and wavelet transforms. Feature extraction and classification methods based on features vectors derived using the above processing techniques are also discussed. These include Mahalanobis distance, support vector machine (SVM) and extreme learning machine (ELM) classifiers. Examples where the proposed methodologies have been successful in classifying TPIs and DCE-MRIs are discussed. Identifying commonalities in the structure of such heterogeneous datasets can lead to a unified multi-channel signal processing framework for biomedical image analysis. The proposed complex valued classification methodology enables to unify entire datasets from a sequence of spatial images taken at different time stamps; this is of interest from the viewpoint of inferring disease proliferation. The approach is also topical to other emergent multi-channel biomedical imaging and of relevance across the biomedical signal processing community.

*Key words:* THz, complex extreme learning machine, quaternary classification, Lagrangian, multiclass classification

## 1. Introduction

The aim of this work is to provide a brief account of recent advances in time series analysis and imaging, leading to the identification of commonalities between TPI and DCE-MRI imaging modalities as both approaches are complementary in their ability to identify and assess disease proliferation. A further aim of the work is to suggest some future directions for machine learning approaches that potentially lead to the automation of diagnostic processes. To clarify these concepts, the paper is structured as follows: Section 1 provides an introduction to THz-transient spectrometry as this is the more well-established modality for building THz imaging systems as well as an account of recent advances in MRI clarifying commonalities in both systems when inferring de-excitation lifetimes at the molecular level. In section 2, the techniques of THz pulsed imaging and DCE-MRIs are examined, together with the imaging modalities that are employed and the type of data that are acquired. We introduce the image formation in relation to THz and DCE-MRI datasets involved in this research, discuss their properties and acquisition parameters, represent their experimental setups, and highlight advantages and drawbacks of both type of images. Additionally, sparse data acquisition methodologies are discussed that can lead to an accelerated data in acquisition. This is currently most relevant to MRI in clinical practice, but can benefit the TPI community, especially if such systems are to undergo clinical trials. Section 3 discusses generic signal de-noising methodologies, applicable to both systems and feature extraction methods using linear transforms. The above discussions are effectively focusing on robust feature extraction from a single pixel perspective. We also discusses recent advances in different classifier methodologies, with an emphasis in complex ELM approaches. The methodology may be naturally extended to multi-pixel or

---

* X.-X. Yin, Email: xiaoxia.yin@vu.edu.au

voxel images. In addition to supervised learning to be represented, the current clustering techniques to segment terahertz images are reviewed briefly. In section 4, we present current DCE-MRI image analysis algorithms. A brief discussion on imaging algorithms relevant to both modalities is provided via an outlook into future design of tensor and Clifford algebra based feature. Extensions to multi-channel classifiers are afforded, as these are necessary to account for specific geometrical features observed across an image and enable data fusion from heterogeneous sources. In addition, such multi-channel approach enables the fusion of information acquired from multiple images at different time stamps, thus potentially elucidating disease proliferation. This section also discusses image registration issues. Section 5 provides some concluding remarks. The work aims to highlight progress towards a generic framework for the automated quantitative assessment of disease proliferation using both sensing modalities.

## 1.1. *Concise introduction to fundamental physicochemical processes associated with interactions of waves with matter across the THz region of the EM spectrum*

Investigations at the terahertz (THz) part of the electromagnetic (EM) spectrum loosely defined between 100 GHz-10 THz are of much relevance to the biological sciences, because complementary information to traditional spectroscopic measurements on low-frequency bond vibrations, hydrogen bond stretching and torsions in liquids and gases may be obtained (Fig. 1). The vibrational spectral characteristics of bio-molecules, which lie in this range (wavenumbers between 3.3–333 cm$^{-1}$) make T-ray imaging systems a promising sensing modality for clinical diagnosis. Since THz photons, (or T-rays), have significantly lower energies (e.g., only 1.24 meV at 300 GHz) than X-rays, they have been considered by many as non-invasive. Although nonlinear interactions between biological tissue and coherent THz radiation have been predicted by Fröhlich [1] and experimentally verified by the careful work of Grundler and the analysis of Kaiser [2] in the '90s, the widely held view at the moment is that any measurement technique that operates at THz frequencies should be evaluated using current guidelines on specific absorption rates; these are only associated with the thermal effects of the radiation with the tissue so from a clinical perspective, such irradiation should be considered as non-invasive. Such view is also further supported by noting that, the Gibbs free energy conveyed in the THz light beam is insufficient to directly drive chemical reactions. For example, the molar energy at a frequency $f$ of 100 GHz would be given from $E = Nhf$ where $N = 6.023 \times 10^{23}$ mol$^{-1}$, (Avogadro's number), and $h = 6.626 \times 10^{-34}$ Js (Planck's constant), resulting in a calculated value of only $E = 0.04$ kJ mol$^{-1}$ which is so low (approximately 100 times lower than the amount of molar energy required for ATP hydrolysis) that for most practical purposes we may assume that the interference with biochemical processes would be minimal.

Further advantages of performing imaging based on the optical properties of biological tissue with THz radiation are the improved penetration depth within the tissue and the comparatively lower scattering than infrared light. Organ differentiation on the basis of tissue water content using microwave transmission or reflection measurements is most of the times impractical because the diffraction limited minimum spot size related to a free-space beam is rather large, and as a consequence there is significant beam spillover around most tissues and organs. This has limited the further proliferation of microwave imaging techniques to the biomedical field.

From a technological point of view, THz imaging is an emergent complementary imaging modality of much interest within the biomedical community. Its proliferation has been somehow delayed because it often needs to compete with positron emission tomography (PET) imaging that is capable of picomolar sensitivity but has poor spatial resolution and magnetic resonance imaging (MRI), which provides millimolar sensitivity with high spatial resolution. A diffraction limited imaging system operating at 2 THz would have a spatial resolution of 150 $\mu$m, which may be considered limiting for many biomedical applications for which this imaging modality offers niche applications (e.g. differential imaging of cancer cells in breast tissue of pregnant or lactating women). From a clinical perspective, tumours need to be identified at the earliest possible developmental stage and unless suitable THz super-resolution techniques can be developed, it is unlikely current systems will be adapted by clinicians. If, however, imaging systems with sufficient SNR could be developed to operate at 10 THz, these would in principle have an attainable resolution of 30 $\mu$m, which potentially have a resolving power just about sufficient for such applications. An additional complication of this imaging modality is that since 70% of the human body is composed of water, a large proportion of the excitation energy would be significantly attenuated. As a consequence, the resultant spectra in many biomedical experiments may only be unambiguously resolved after the application of elaborate post-processing techniques.

## 1.2. *Introduction to dynamic contrast enhanced MRI (DCE-MRI)*

The principle of magnetic resonance imaging (MRI) was discovered in the late 1940s, through pioneering experiments by Sir Peter Mansfield while he was a student at Queen Mary College, University of London under the supervision of D. H. Martin and independently by Paul Lauterbur while he was at the University of Pittsburgh, the Mellon Institute of Industrial Research and subsequently the State University of New York at Stony Brook after following the work of Robert Gabillard on Nuclear Magnetic Resonance (NMR). It was only, in 1980, however, that MRI was introduced as a new diagnostic modality and a lot lat-
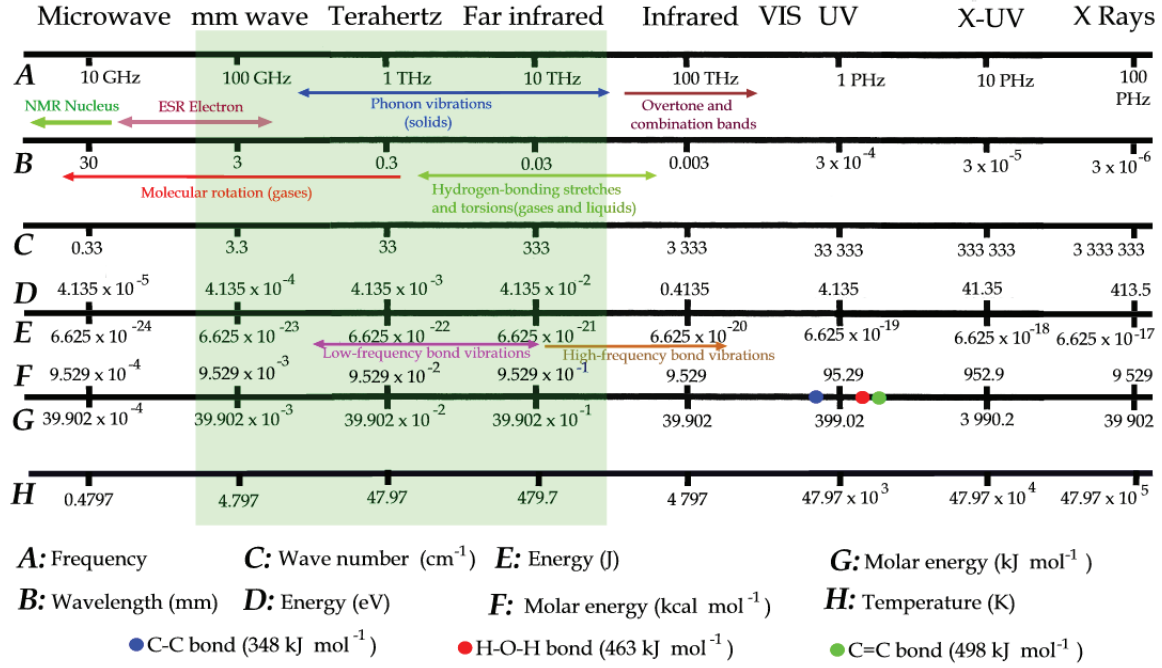
Fig. 1. Multidisciplinary interpretation of the electromagnetic spectrum.

er that it gained wider acceptance as an imaging tool for a diverse range of biomedical disciplines such as neurology, oncology, obstetrics and gynaecology. In a clinical setting, it is now routinely used in cardiovascular, musculoskeletal, gastrointestinal and liver imaging as well as in neuroimaging, providing information on their physiological status and pathologies. In this respect it also complements NMR.

Note that MRI de-embeds structural details of the various organs on the basis of the observation of hydrogen atom (proton) de-excitation rates as they arise following an excitation by an oscillatory radio signal within a magnetic field. The energy emission stemming from the spinning hydrogen molecules is determined by two time constants, $T_1$ and $T_2$ and the contrast between different tissues is determined by the rate at which excited atoms return to the equilibrium state. The radio signals can be made to encode position information by varying the main magnetic field using gradient coils, enabling the formation of images. Simple $T_1$ and $T_2$ weighted images are very common in many medical applications. An important advantage that MRI has over its computed axial tomography (CAT) counterpart is that it avoids the deleterious effects associated with X-ray irradiation.

A significant advance in MRI technology for the non-invasive assessment of disease proliferation has been witnessed through the use of exogenous contrast agents, the so-called dynamic contrast enhanced MRIs (DCE-MRIs). Note that DCE-MRI enables the detection of tumour anomalies with high sensitivity [3]. The crucial advantage of DCE-MRIs over standard MRIs is that the DCE-MRI modality provides 3D spatial lesion information as well as temporal information regarding the progression of lesions.

Furthermore it provides information by showing variations in contrast agent uptake rates and enables a more accurate assessment of the extent of lesions and new opportunities for their better characterisation [4, 5]. From a classification perspective, DCE-MRI produces a sequence of three-dimensional (3D) patterns recorded at different time instances. These datasets are therefore four-dimensional, with three spatial dimensions and a quantization in the time domain defined by the image interval lapse time. The detection of anomalies in spatiotemporal datasets is an emergent interdisciplinary topic that requires the development of completely new software tools [6]. Furthermore, as discussed in [7–10], analysing spatiotemporal patterns is critical for the correct identification of tumour anomalies in DCE-MRIs, establishing whether they are malignant or benign. Finally, it is worth noting that currently clinical MRI stands at the cross-roads between some important technological developments. These include the recent advances in higher field (3 Tesla) imaging systems as well as the more experimental low field (milli-Tesla) systems which have cryogenically cooled phased array detectors. Detail in the images produced by these new experimental modalities differs from that found in the traditional 1.5 T systems, requiring additional time by trained experts for their interpretation. Such problems can compromise their further proliferation unless automatic image classification algorithms can be developed.

Progress in machine learning offers new opportunities for automated biomedical data mining and disease diagnosis as it can potentially simplify the process of searching through large volumes of medical images for features selection and identification, as well as tumour screening. In addition, it

can also potentially provide associations and correlations through time series analysis of datasets, thus elucidating disease proliferation [11–16]. Image processing techniques can be used to extract quantitative information on lesion morphology, volume and kinetics, as well as to distinguish viable from nonviable tissue [4, 14]. Techniques for processing large volumes of medical image datasets with high dimensionality are not sufficiently mature, however. Experts often distinguish tissue states on the basis of tumour information from radiological reports by characterizing lesions either as malignant or as benign [4, 17–20]. Such practice is subjective, relying on the availability of experts and occasionally inaccurate, as it involves a binarization step of the classified output without taking into consideration intermediate values as a fuzzy-set expert system would do (it also incorporates a slight bias towards false-positives to avoid mistaken diagnoses as this could potentially tarnish an expert's reputation). A further disadvantage of this approach is that it can be slow and therefore costly, inducing additional pressure loads in otherwise already overloaded health systems worldwide. In addition, it is also worth noting that alternative, tumour detection methodologies based on analysing a series of two-dimensional texture features as local descriptors using a sliding window, have a major shortcoming in that they are unable to take into consideration more complex morphological features of tumour anomalies across the entire tissue volume [10, 14, 21].

Furthermore, there are other pressing needs for the further development and wider proliferation of multi-channel machine learning algorithms for the biomedical community. In DCE-MRI, for example, motion correction software often needs to be employed [22]. Correlations with breathing, provided from an additional channel source (e.g. an optical fibre based plethysmograph) could assist pixel de-blurring at a post-processing stage, minimizing artefacts [23]. Hyperspectral imaging is also another emergent modality in biomedical screening (e.g for skin cancer detection), requiring such multi-channel signal processing. From a signal-to-noise ratio (SNR) image quality perspective, for each pixel, an improvement is only possible by using a stronger excitation source per spectral bin, by improving on the detector responsivity and noise floor, and by integrating over a longer time at each pixel or voxel. Equipment manufacturers argue that there is really no substitute for increased integration time to perform the de-noising process. Broadband signals, however, enjoy the Fellgett multiplex advantage, which makes use of the broadband nature of a short pulse measurement modality to provide superior clarity per pixel for a set measurement integration time when compared to successively scanned frequency domain investigations using continuous-wave source measurement modalities. It is not uncommon, therefore, that in order to speedup measurement time in many MRI applications, different software approaches are considered by limiting the fidelity (number of pixels or voxels) or reducing the number of tomographic projections. Such practice, however, can lead to image feature artefacts if sampling is not performed following Nyquist's criterion in the spatial domain [24, 25]. A pre-processing step that can reduce the dimensionality of the data-set by compressing it to more parsimonious representations without distorting it can potentially minimise the dimensionality of the input dataset presented to a classifier. This can help in improving its classification accuracy and generalization ability. Furthermore, an additional advantage from compression is that it is advantageous from a signal-to-noise ratio perspective as the co-averaged signal components in each spectral bin are always in-phase whereas the noise component are out-of-phase and thus suppressed. Image reconstruction and registration are further discussed to more detail in the third section of this paper.

## 2. Biomedical imaging techniques and modalities for THz radiations and DCE-MRIs

Medical imaging is the technique and process of creating visual representations of the interior of a body and seeks to reveal internal structures hidden by the skin and bones, as well as to diagnose and treat disease. This section incorporates in depth study on the design, clinical applications and research potentials of the two highly specialised imaging modalities: terahertz pulsed imaging and DCE-MRIs. Emphasis is on technology development but extends to the science of image formation along with the properties and acquisition parameters of theses two imaging modalities, with a focus on the physics and mathematics of their imaging devices and systems.

### 2.1. *Time-dependent techniques using terahertz radiation*

Although much of the pioneering work in building interferometric spectro-radiometers and other continuous wave measurement systems at the THz part of the spectrum took place at Queen Mary College over a period of almost 30 years under the guidance of D.H. Martin [26], it was only during the past two decades that THz science and technology has literally flourished as a universally accepted new sensing modality. This has been largely due to the advent of time domain spectroscopy (TDS) with ultrashort-pulse laser sources. These systems enable time-resolved 'far-infrared' (FIR) studies for biomarker identification, which through explorative spectroscopic investigations may eventually lead to novel imaging applications in the submillimeter part of the spectrum. T-rays have significant potential in advancing both in *in vivo* and *in vitro* biosensing applications [27–29] due to their relatively non-invasive interaction with biological tissue. Furthermore, several biomolecules have several characteristic 'fingerprint' resonances due to overtone and combination bands [30, 31].

Notably, THz-TDS is a time-domain technique similar to the well-known pulsed radar sensing modality, where the time gated reflections are analysed directly in the time domain by observing their attenuation, phase delay and tem-

poral spread after interacting with matter. Their temporally good definition can provide localization of tissue interfaces on the basis of their different refractive index (the real part associated with impedance mis-match) or through the complex part which is associated with the attenuation due to the number of absorbers and their extinction coefficient. Studies in reflection geometry also enable the indirect assessment of sample or layer thickness, as well as in determining the position of embedded unknown objects, etc. [27]. Pulsed terahertz (THz) wave technology has also been applied extensively in biosensing. The pioneering investigations in biomolecule characterization were performed by the Aachen group [32] and Jepsen's group [33]. These were followed by a subsequent avalanche of investigations by other researchers worldwide [34–36]. An interesting example is that of an affinity biosensor monitoring the binding between biotin and avidin molecules on supported membranes composed of biotin layers on a quartz surfaces treated with octadecanol, as proposed by Menikh et al [37]. In that work, an amplified detection of biotin-avidin binding was very clearly observed through the dithering of the samples in a THz beam. This was attributed to the conjugation of agarose particles and avidin molecules and a change in contrast due to a change of refractive index resulting from the chemical binding process [30, 38]. As avidin has a very strong affinity for biotin and is capable of being bound to any biotin-containing molecules, the developed detection technique is quite generic and can potentially be used to detect DNA hybridization and antigen-antibody interactions [30]. Fischer *et al.* [39] was able to reliably distinguish between two artificial RNA single strands, composed of polyadenylic acid (poly-A) and polycytidylic acid (poly-C) from their different THz spectral transmission responses. In that study poly-C samples consistently showed stronger signal attenuation than poly-A samples.

## 2.2. *Frequency dependent terahertz spectroscopy*

In the THz part of the spectrum, many molecules have characteristic 'fingerprint' absorption spectra [27]. Substances in the condensed phase are held together by either ionic, covalent or electrostatic forces, and therefore the lowest frequency modes will be associated with intermolecular motion [40]. The interaction between THz radiation and biological molecules, cells, and tissues can be understood using assumptions of propagation of an angular spectrum of plane waves through the material [41]. Following standard dielectrics theory postulations, a medium may be characterized in terms of its permittivity $\varepsilon$ (the ability of the medium to be polarized) and conductivity $\sigma$ (the ability of ions to move through the medium). At higher frequencies, transitions between different molecular vibrational and rotational energy levels become increasingly dominant and are more readily understood using a quantum-mechanical framework [42]. Terahertz pulse spectroscopy provides information on low-frequency inter-

molecular vibrational modes [43].

### 2.2.1. *THz radiation absorption and detection in tissue*

Terahertz radiation interacts strongly with polar molecules, a prime example being water. [44]. Polar water molecules are active in the infrared region and have various vibrational modes [45]. In the mid- to far-infrared, the vibrations involve combinations of the symmetric stretch ($\nu1$), asymmetric stretch ($\nu3$), and bending ($\nu2$) of the covalent bonds. The vibrations of water molecules may be thought of as restricted rotations, resulting in a rocking motion, as shown in Fig. 2(a). In liquid water, since hydrogen bonds are much weaker than the covalent bonds (intra-molecular), their bond lengths are much longer (1.97 Å versus 0.96 Å), as shown in Fig. 2(b). Steric effects from dipole moments in water clusters vary according to hydrogen proximity and as a consequence, shifts in rovibrational modes at THz frequencies are encountered. Furthermore, these shifts are expected to be loosely correlated with different water potential values, which surrogately affect its ability to interact with the surrounding molecules. This has further important ramification on the way proteins influence the state of water and can lead to further understanding of the function of hydration shells in proteins [46, 47]
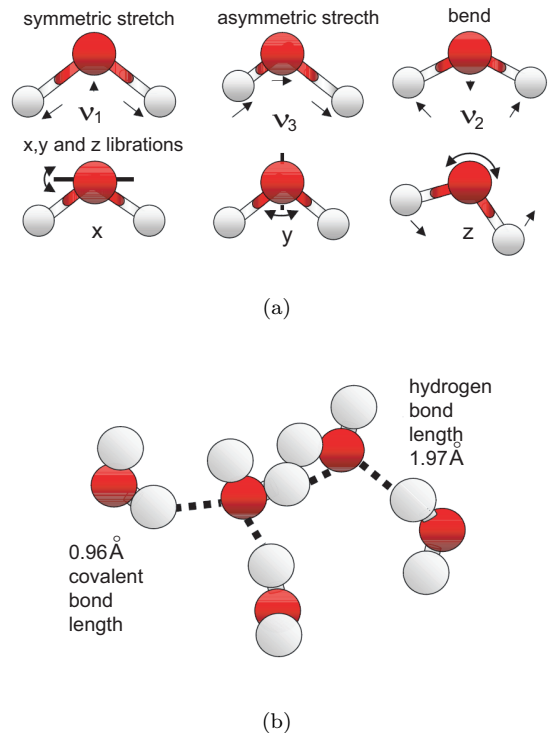


(a)



(b)

Fig. 2. (a) The main vibrational modes in water. (b) A schematic diagram illustrating the differences between intra- and inter-molecular bonding in water. After [45].

THz time-domain spectroscopy provides a direct measure of the real and imaginary components of the permittivity. A Debye relaxation model can be used to analyze

the strong absorption of terahertz radiation in polar liquids at least up to 1 THz [31, 48]. This model can be directly related to the associated intermolecular dynamics.

Biological tissue is generally composed of polar liquids. Due to the exceptionally high absorption losses of polar liquids at terahertz frequencies and the low source power in TPI systems, it is impossible for the THz radiation to penetrate through biological tissue of any substantial thickness. However, the same high absorption coefficient that limits penetration in tissue also provides extreme contrast between samples at various degrees of water saturation [31]. This property has proven advantageous in the examination of the properties of water uptake and distribution in plants [49, 50], as well as in the evaluation of the severity of burns through the evaluations of necrotic skin samples [28]. In addition, [51] and [52] describe the application of TPI techniques for imaging of basal cell carcinomas (BCC) *ex vivo* and *in vivo*. BCCs typically show an increase in absorption of THz radiation compared to normal tissue. This may be attributed to either an increase in interstitial water within the diseased tissue [53] or a change in the vibrational modes of water molecules through interactions with other functional groups. Systematic studies in tissue identification are reviewed in [31].

### 2.2.2. *Identification of compounds with complex composition*

The identification of pure compounds using molecular signatures with THz-TDS systems is still not straightforward because of the inherently broad spectral signatures in liquids and solids. Nevertheless, there is a growing number of multiply confirmed observations of particular resonant signatures that may be attributed to the presence of many compounds in pure form [54]. Of particular relevance here is the growing interest in studying the conformational structure, binding states, and vibrational or torsional modes of proteins and oligonucleotides [55, 56] through the analysis of spectral features [57]. Different reflection or absorption signatures may also be attributed to a change of density or polarizability, or may indicate a dehydration state, or a denaturing process leading to a new amorphous absorption band or a temperature related absorption band shift. A compilation of readily identifiable spectral signatures of complex biomolecules in an atlas has already been considered at Durham University, and significant progress is being made, yet there is recognition by the THz community that it is unlikely it will have the universal applicability associated with other databases such as HITRAN, because of the variability in the location of the spectral bands observed under different experimental protocols.

There are still, however, several examples of useful studies that may be found in the recent literature. Nishizawa *et al.* [58] illustrated the use of a widely tunable coherent terahertz scanning system for THz transmission spectroscopy to study samples consisting of nucleobases, nucleosides, deoxynucleosides, and nucleotides, to further gain an insight of the composition of RNA and DNA molecules. THz spectra of those samples in crystalline form were measured in the 0.4–5.8 THz range. These studies showed that the molecules have quite different characteristic spectral patterns in this frequency region, furthermore the absorption signature patterns observed were sufficiently clear and reproducible for identifying and discriminating between these molecules. Using pulsed THz spectroscopy [55] it has also been possible to study the low frequency collective vibrational modes of bio-molecules, i.e. DNA, Bovine Serum Albumin and Collagen in the range 0.1 and 2.0 THz. It is generally accepted that for most samples, broadband absorption increases with frequency and a large number of the low frequency collective modes for these systems is also deemed as IR active. Herrmann *et al.* [59] also carried out measurements of THz spectra of Poly(dA-dT)-Poly(dT-dA) DNA and Poly(dG)-Poly(dC) DNA and used new signal processing routines to infer the THz complex refractive index. The resultant spectral features showed that those samples were indeed distinguishable in the range 0.1 to 2.4 THz. Several research groups in Germany and Australia, have also studied the photo-isomerization of retinal chromophores [60, 61] focusing on the conjugated polyene chain of the biologically important chromophore retinal and its low-frequency torsional vibration modes. In that work, the absorption and dispersion spectra of different retinal isomers (all-trans; 13-cis; and 9-cis retinal) in the far-infrared region between 10 and 100 cm$^{-1}$ (0.3 $\pm$ 3.0 THz) were measured by THz-TDS at 298 and 10 K. At low temperatures, it was observed that the broad absorption bands resolve into narrow peaks that directly correlated to torsional modes of the molecule. The study also confirmed that vibrational modes within the molecule can be approximately localized through a comparison of the absorption spectra of different retinal isomers. An alternative important research direction vigorously pursued by Teraview Ltd., Cambridge, U.K., aims to put an end on patent infringements within the pharmaceutical industry by detecting the presence of drug polymorphs [43, 62, 63]. Such studies, for example, have successfully used TPI to examine the variation in the crystalline structure of Ranitidine Hydrochloride polymorphs. Significant differences in the spectra of two different polymorphs were clearly observed at around 1.10 THz enabling their correct identification. A recent account on advances in the identification of crystalline structure of drugs using TPI is provided in [64]. Furthermore, the observation of the crystallization of compounds has also been possible [65].

### 2.3. *Time-frequency dependent terahertz spectroscopy*

Time-frequency analysis methods have been developed to provide very parsimonious parametrizations of time series datasets and in this sense complement well other parametrization schemes performed in either time or frequency domains [66, 67]. The wavelet transform (WT) is a popular technique suited to the analysis of short-duration
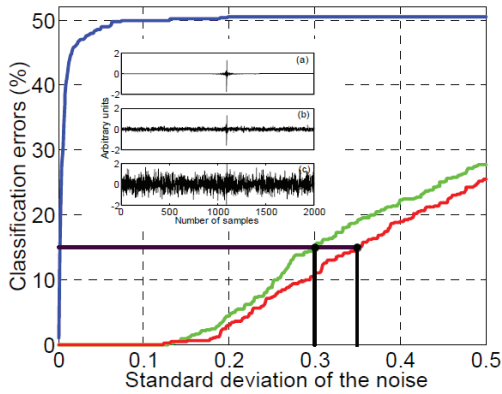
Fig. 3. Classification errors (%) as a function of noise level in the interferograms. Nonoptimized db4 wavelet (green), optimized wavelet (red) and Euclidean distance (blue) classifiers. The inset shows a leather interferogram with (a) no artificially added noise and noise with standard deviation of (b) 0.1 and (c) 0.5. After [73].

signals [68]. It decomposes the time series signal using two filter banks separating the high (detail) and low (approximation) frequency components of the signal assuming a pre-defined mother wavelet function. The approach provides very efficient de-noising capabilities in the presence of Gaussian white noise and has very parsimonious representation. An important feature of this transform is that it is orthogonal so that it enjoys perfect reconstruction symmetry, which enables its inverse transform to reproduce the original dataset without loss of information. This is a particularly important property from a biomedical signal processing perspective as software certification for biomedical purposes should require complete traceability of all the data processing steps. A further development in the biomedical signal processing literature has been the use of adaptive wavelets [69], where the mother wavelet is specifically tailored at each decomposition level (wavelet scale) accordingly, to minimize the least squares error associated with the difference between the transformed signal from its original one. This approach holds great promise for optimizing the extraction of the spectroscopic information contained in each THz pulse transient as well as in THz TPI generally [70–73]. Figure 3 presents the result of this simulated test, in terms of classification errors. To generate this graph, the standard deviation of the noise was varied from 0.001 to 0.5. For each noise level, 250 noisy patterns were generated for each class (lycra and leather). As can be seen, the classification is much more robust to noise when carried out in the wavelet domain than in the original domain. Moreover, the robustness to noise is further increased by the optimization of the wavelet transform.

In addition to the above more elaborate routines, there have also been other examples of studies that incorporate wavelet transform pre-processing routines for signal-to-noise-ratio enhancement and classification of THz spectra [28, 74]. Such pre-processing steps enabled the successful discrimination of cancerous from normal tissue in wax-embedded histopathological melanoma sections as well as

the classification of dentine and enamel regions in teeth [70]. It is nowadays generally accepted that the performance of a classifier based on the output of a wavelet filter bank is better than that of an Euclidean distance classifier in the original spectral domain [73]. Finally, an alternative very promising approach for the modelling of de-excitation dynamics which has its origins to the theory of complex dielectrics is through the use of fractional order calculus and the fitting of fractional order models. In this approach, the time series experimental datasets are modelled using very parsimonious pole-zero expressions associated to dynamics of resistive, capacitive or inductive networks [75–77]. Although the fractional-order system identification literature is still at its infancy, it promises to provide much lower residual errors in the identified models thus significantly advancing the science of Chemometrics which is essential to the further advancement of the discussed biomedical investigations. The approach can account for spectral shifts in amorphous materials as well as de-embed solvation dynamics.

## 2.4. A brief introduction to experimental set-ups for THz trans-illumination

THz imaging can be remarkably informative regarding a sample's composition. The Fourier transform of the associated time domain waveform over a certain spectral range allows the calculation of the frequency dependent refractive index and absorption coefficients of the sample. If the Fourier transform is performed in real time using dedicated hardware, it becomes possible to extract the above parameters also in real time. Since wavelengths are longer in the THz part of the spectrum, there is sufficient phase stability in the experimental apparatus, this enables the extraction of phase information by varying the time delay between the THz wave and the probe beam [27]. Since some materials are transparent to THz radiation, it is occasionally feasible to measure transmission responses and acquire spectral information. Reflectance imaging is also straightforward, and through their combination, a spectral absorbance may be inferred. This is not always possible at the infrared and optical parts of the spectrum where errors due to scattering of shorter waves due to the surface roughness of the samples preclude direct calculations of absorbance. Elementary signal analysis may also be used (e.g., differential absorption) to produce informative contrast images that can be invaluable to the evaluation of disease proliferation.

Using continuous wave systems, there is a variety of instruments that may be assembled using quasi-optical active and passive components. The AB Millimetre vector network analyser, if available, is the preferred choice for continuous wave measurements with significant signal-to-noise ratio per spectral bin all the way up to 1.2 THz although it is not as user friendly for extracting scattering parameters as other commercially available solutions which operate at much lower frequencies. An account of different topologies

using null-balance methods can be found in [78] whereas polarimetric measurements for dichroic samples should be ideally performed using the topologies discussed in [79, 80] or Fabry-Perot structures, e.g. [81]. Alternative broadband experimental configurations may include Mach-Zehnder or Martin-Puplett configurations as discussed in [50]. When high power per spectral bin is needed, THz imaging may also be performed with high-power THz sources under pulsed scanning mode and pulse-gated detection using large scale facilities (e.g. Jefferson lab, FELIX etc) but at significant cost. Currently, however, bio-medical investigations with such facilities lag behind investigations performed by the semiconductor community.

An important advantage of time-domain systems over their continuous wave counterparts that are plagued by etalon effects is that of being able to perform time gating of the pulses. This is possible as long as the multiple reflections in the measurement system are sufficiently far away so as not to be mixed with the molecular de-excitation signals of the sample. The typical time-resolved THz spectrometer used in most of the studies discussed so far utilize a short coherence length infrared source (centered at around 800 nm) to generate a sub-100 femtosecond duration pulse train with repetition frequency of around 80 MHz. Each infrared pulse, is split into separate pump and probe beams. The pump beam is used to excite an optical rectification crystal, which acts as a T-ray emitter, and the T-rays produced (duration around 200 fs) are collimated and focused onto a sample by a pair of parabolic mirrors. The T-rays emerging from the sample are re-collimated by another pair of mirrors, before being combined with the probe beam in a T-ray detector crystal. As a result, the modification by the sample T-ray and the probe beams propagates through the THz detector crystal co-linearly. The pump beam, which is also transmitted through a chopper, travels through an optical delay stage that is modulated accordingly, so that the pump and probe beams arrive at the detector in a time-coincident manner. The electro-optic detector crystal produces an output that is proportional to the birefringence observed from the interaction of the THz pulse with the time-coincident infrared pulse replica within the crystal. This output is proportional to the T-ray response of the sample and this signal is measured with the use of a balanced optical photo-detection scheme. A lock-in amplifier (LIA) is also used to demodulate the signal, and this avoids $1/f$ (flicker) noise problems that are present in this detector-limited measurement scheme. THz-TPI is performed through a 2D raster scan after translating the sample in both the $x$ and $y$ direction, while keeping it at the focal plane of the parabolic mirrors. A typical setup [82] is shown in Fig. 4.

It is also worth noting that in all of the above experimental set-ups one needs to always consider that there may also be additional pseudocoherence errors because different parts of the beam across its aperture travel different paths through different regions of the sample (if this is of non-uniform thickness), interfering constructively or destructively with each other when they recombine. A recent
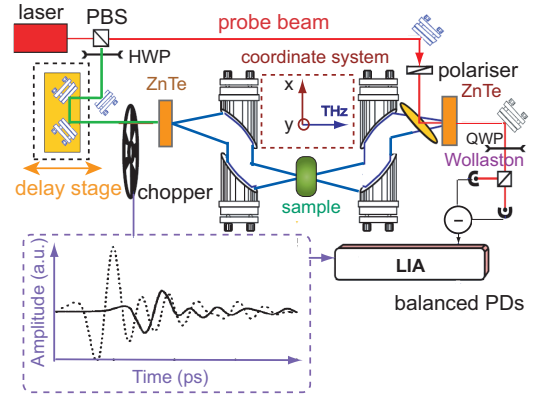


Fig. 4. A schematic experimental setup for electrooptic transmission terahertz imaging with ZnTe as EO generation and detection, illuminated by a femtosecond laser.

account of advances in THz metrology discussing errors in both continuous wave as well as THz-transient systems can be found in [83]. Such errors are endemic to much of the THz literature although this is not extensively discussed. Management of these artefacts and their relevance to imaging applications is therefore an open issue requiring further consideration.

The resultant measurement at each pixel position of an image is an entire time-dependent waveform. Therefore, the result from TDS-TPI is a three-dimensional (3D) data set, which then can be potentially mapped to two-dimensional (2D) images [84], where structural and compositional discrimination based on a sample's optical properties may be conveniently performed using pattern recognition algorithms. In the following section, sample responses from multiple THz spectrometry experiments are extended to provide a pattern recognition framework . The proposed approach extends the range of application of pattern recognition to emergent sensing modalities [85].

## 2.5. DCE-MRI imaging techniques and modalities

**The diagnosis, grading and classification of tumours has benefited considerably from the development of magnetic resonance imaging (MRI). It is now essential to the adequate clinical management of many tumour types. The ability of MRI to demonstrate tumour morphology and the relationships of malignant lesions to neighbouring structures provides essential clinical information for both clinical management and surgical planning. Magnetic resonance has innate advantages in these applications enabling clear delineation of normal anatomical structures and organs and, in most cases clearly delineating and identifying pathological change. please help me rewrite this paragraph. this is from some other authors work.**

As a high-performance imaging modality, DCE-MRI is now widely used in the diagnosis of cancer and is becoming a promising tool for monitoring tumour response to treat-

8

ment [86]. Dynamic contrast enhancement patterns can be affected by a wide range of physiological factors which include vessel density, blood flow, endothelial permeability and the size of the extravascular extracellular space in which contrast is distributed [86, 87]. The crucial difference from traditional medical imaging (i.e. X-rays) is that the DCE-MRI modality provides 3D spatial information about lesions as well as temporal information about lesion physiology (showing variations in contrast agent uptake rates), allowing for more accurate assessment of lesion extent and better lesion characterisation [8].

Typically, DCE-MRI images are acquired with the use of a conventional gradient echo (GRE) pulse sequence to repeatedly image a volume of interest after injecting a contrast agent, such as gadolinium diethylenetriamine pentaacetic acid (Gd-DTPA) into the patient's blood stream. The DCE imaging employs a full k-space sampling strategy, (where the k-space relates to the associated wavenumber, a terminology originally established by the semiconductor industry). Three dimensional (3D) volume acquisition slice profiles are generally rectangular and slices are always contiguous. This means that signal derives uniformly from all tissue in each slice, without cross-talk.

One of the biggest advantages of the gradient-echo pulse sequence is that it can be performed quickly enough to enable 3D Fourier Transform (3DFT) data acquisitions. In 3DFT imaging, a volume or slab of tissue is excited, rather than merely a thin slice of tissue. It means the 3D MRI data acquisation consists of three different phase encoding directions: the transaxial plane, the sagittal plane, and the coronal plane. Typically, 3D image sets are obtained sequentially every few seconds for up to 5–10 minutes. There is always a trade-off between spatial (sRes) and temporal (tRes) resolution. Usually, most radiologist's clinical protocols show a preference for scans at high sRes allocating only 1–2 min for tRes data acquisition [88].

A typical DCE-MRI dataset used for the image analysis consists of one baseline 3D MR image which is used as a reference before contrast agent injection. This is subsequently measured in a repeated manner to acquire post-contrast images at the second, third, till sixth time slices. Each time slice has a typical time interval equal to 60 seconds.

Following the terminology introduced independently by Ljunggren [89] and Twieg [90] we shall refer to the, $k$-space to denote the spatial (either 2-D or 3-D) frequency domain of the imaging system. Within the context of temporary image processing the $k$-matrix, is composed of digitized MR signals stored during the data acquisition process before any reconstruction computations. The complex data entries are associated to a pulse sequence of accurately timed radio frequency and gradient pulses.

In clinical practice e.g during a DCE-MRI mammogram, it is desirable to reduce the signal acquisition time; this is normally achieved by undersampling the $k$-space. This may achieved by adopting a random partial k-space updating [91] protocol. The HASTE sequence which samples half the k-space [92] is now routinely used in clinical MRI.

Aliasing from sampling the k-space below the Nyquist rate, however, introduces imaging artifacts. Since there is always a need for better tRes while preserving adequate S-NR and sRes, several groups [93–95] have shown that it is possible to accelerate DCE-MRI (without employing parallel imaging) by a factor of ten using compressed sensing (CS) based for image reconstruction as proposed in [24]. The approach allows filling of missing k-space data using a constrained optimization technique to interpolate the values between under-sampled adjacent data points in the spatial domain.

Research by Yin et al. [96] is based on the broad principles of compressed sensing and makes use of the fact that, when under-sampling the $k$-space, it is possible to use variable density sampling schemes in a Cartesian coordinate system to widely distribute the resulting artifacts and reduce their visual impact. Such approach was further explored using a model-based method for the restoration of MRIs with sparsity representation in a transformed domain, e.g. spatial finite-differences (FD), or discrete cosine transform (DCT). The reduced-order model, in which a full-system-response is projected onto a subspace of lower dimensionality, has been used to accelerate image reconstruction by reducing the size of the linear system associated with the measurement space. The singular value threshold technique [97] (SVT) was used in the denoising scheme to reduce and select the model order of the inverse Fourier transform image, and to restore multi-slice breast MRIs that have been compressively sampled in $k$-space. Restored MRIs with SVT de-noising show reduced sampling errors compared to direct MRI restoration methods via spatial FD, or DCT. The difference image related to IT shown in Fig. 5(b) contains a relatively large number of noisy (error) pixels that are located around the boundary of the imaged section. Reconstruction with IT shows also some blur at the image edges. In contrast, the reconstructed image using SVT denoising illustrated in Fig. 5(a) shows a reduced number of error pixels compared to the reconstructed image in Fig. 5(b).

## 2.6. *Advantages and disadvantages of T-rays and DCE-MRIs*

Advanced terahertz pulsed imaging (TPI) and DCE-MRIs are becoming widely available in conventional clinical practice, where data acquisition and analysis are comparable despite inherent differences in signal production and mechanism of tissue contrast. One of the primary advantages of THz imaging over competing techniques including MRIs is the availability of spectroscopic data within a potentially crucial frequency band. Unfortunately, the responses of many biological tissues are unknown in this band. A significant amount of research is to characterize tissues, such as DNA [55, 58, 59]. An associated problem is the development of computer aided diagnostic algorithms for interpreting the multispectral images obtained by T-ray imaging [98]. A number of authors have considered
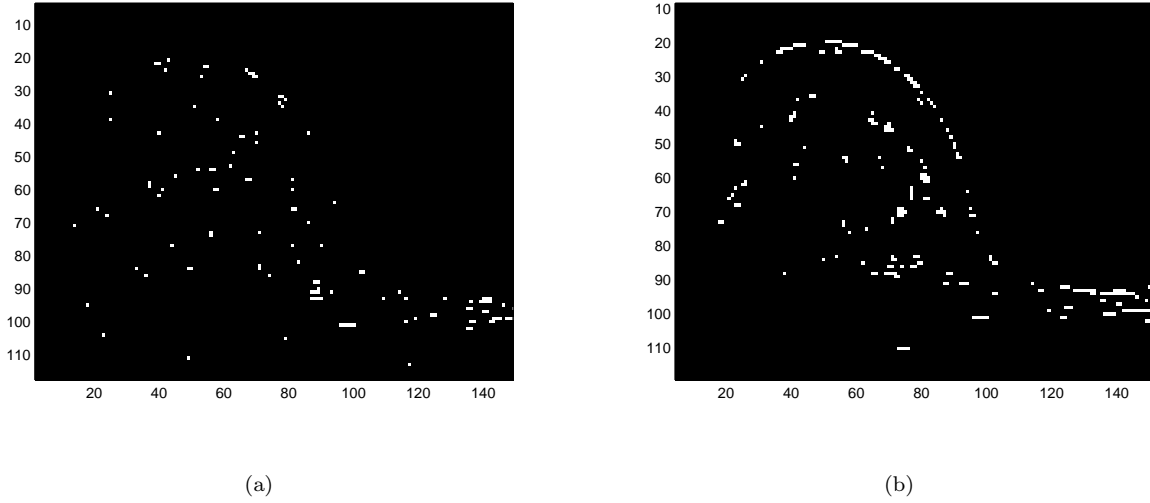
Fig. 5. Illustrations of resultant experiments at the 26th layer, (a) the difference image segment between the measured MRI and reconstructed image using SVT for denoising. (b) The difference image segment between the measured MRI and transformed image from sampled $k$-space.

this question by fitting the measured data to linear filter models and using the filter coefficients as a means to classify tissue types [99]. One of the most important potential applications for terahertz technology is the detection and identification of biological and chemical agents [100]. Although T-rays can be used to image tumour microvasculature, more reports on the feasibility study using TPI are focused on imaging breast tumours [101, 102] and skin cancer [103], due to the absorption of THz waves by water that is found in biological tissue. A recent review has been carried out by Yu *et al.* [104], where investigations relating to the potential of terahertz imaging and spectroscopy for cancer diagnosis has been highlighted. An important progress in THz tumour image was reported by Huang *et al.* [105] in 2006. In their work, they provided an in vitro demonstration of gold nanorods as novel contrast agents for both molecular imaging and photothermal cancer therapy. As a result of the strongly scattered red light from gold nanorods in dark field, observed using a laboratory microscope, the malignant cells are clearly visualized and diagnosed from the nonmalignant cells.

Dynamic contrast-enhanced magnetic resonance imaging (DCE-MRI) is the acquisition of serial MRI images before, during, and after the administration of an MR contrast agent. Unlike conventional enhanced MRI, which simply provides a snapshot of enhancement at one point in time, DCE-MRI permits a fuller depiction of the wash-in and wash-out contrast kinetics within tumors. Depending on the analysis approach chosen, measurements may be derived from signal intensity data, or more commonly, signal intensity data are transformed into contrast concentration data prior to analysis [106]. Different from terahertz measurements that the impulse function for tumour is very different to that of normal adipose (fatty) tissue, the resultan-

t changes in signal intensity taken from DCE-MR images are different for healthy and tumour tissues according to the different degree of absorption of contrast agent. Different from terahertz measurements that are the function of continuous time, DCE-MRIs are acquired at several time frames that form low temporal solution. This forms limitation in accurate reconstruction of tumours after projecting 4D images to 3D as illustrated in the section "DCE-MRI imaging analysis".

## 3. Analysis & classification of THz imaging data

T-ray pattern classification aims to select a sub-set of significant features in the image data set, without incurring a dramatic loss of information. Through pattern analysis, any relations, regularities, or structures associated with the measured T-ray response can be found. By detecting patterns, a T-ray classification system should be able to automatically make generalizations on its input space on the basis of its training set [107]. Such approach is particularly useful within a laboratory automation context. Consequently, complete automated solutions should be seen as composed of three different modules that may be individually optimized for particular samples and data sets: the data acquisition imaging spectrometer module, the data de-noising pre-processing module and the classifier module. Depending on the type of sample, tuning may be tailored for each module before the learning process is initiated.

### 3.1. *Pre-processing for THz-TDS pulses*

During pre-processing, input data vectors need to be grouped together into sets of feature vectors [85]. The choice

10

of parameters for grouping is fundamental to the subsequent performance of the classifier. Data pre-processing aims to isolate the real T-ray responses from the effects of amplitude and phase noise associated with the pulse to pulse stability of the source, laser beam pointing stability and detector shot noise, thus reducing artefacts that could compromise the classifier performance. Co-averaging multiple measurements by moving the scanning delay line unidirectionally several times through its central maximum (slow-scan mode) or changing the lock-in time constant (fast-scan method) improves signal-to-noise-ratio per pixel but at the expense of significantly increased measurement time and image acquisition. Since improvement in signal-to-noise ratio is proportional to the square root of the number of co-averaged time-domain responses; this approach significantly limits the integration time that may be budgeted for each pixel. Furthermore the approach is unsuitable to the analysis of samples whose THz response is time-dependent e.g. drying. Signal processing can partly alleviate some of these issues. Window apodization for example reduces frequency domain Gibbs ripple due to the data discontinuities at the edge of the recorded time domain interferograms. Optimization of the apodization function is now possible using algorithms accounting for the asymmetry of the propagating femtosecond THz pulses [108].

Multiresolution techniques such as wavelet transforms are particularly effective to further de-noise mean-centered apodized interferograms. A typical de-noising procedure consists of decomposing the original signal using DWPT or DWT [109–111], thresholding the detail coefficients, and reconstructing the signal by applying the appropriate inverse transform (IDWT or IDWPT respectively). For the de-noising of femtosecond THz transients, a three-level decomposition is usually sufficient [112] and unnecessary computational load associated with more decomposition levels can be avoided. Fig. 6, illustrates the process [113].

An alternative promising pixel de-noising method involves the use of wavelet power spectrum estimation techniques (WPSET), as discussed by Kim et al. [114]. This approach may remove spectral artefacts without distorting spectral features in a more efficient manner. The author's application of WPSET to the transmission spectrum of water vapor verified the effectiveness of the approach. This is a nonparametric approach based on a wavelet representation of the logarithm of the power spectrum [115]. Alternative signal pre-processing methods for de-noising include base line correction [116], smoothing [117], first and second derivative [117, 118], multiplicative scatter or (signal) correction [119], and standard normal variate analysis[120], Although all these methods have their own merit under different experimental conditions, one may argue that wavelet de-noising has the widest applicability [121].

From an imaging perspective, the discrete cosine transform (DCT) using Wang factorization, Lee's power of two block lengths DCT scheme, Arai's scheme, Loffler's algorithm or Feig-Winograd factorization [122–125] are particularly useful. The attractiveness of the DCT algorithm
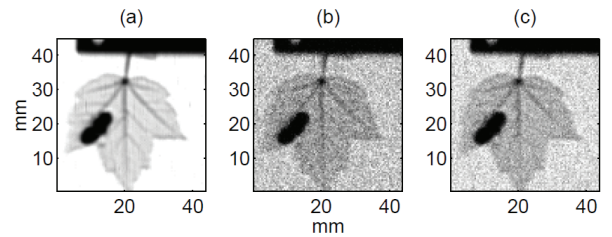


Fig. 6. Image of an insect on an oak leaf obtained by terahertz pulse imaging. The image is produced by plotting the peak value of the response for each pixel. (a) Raw image. (b) 3 dB SNR image corrupted by noise such that the SNR was. (c) Reconstructed image after de-noising using a Coiflet wavelet filter decomposition of order 4 where the average SNR is 10 dB greater than in (b). After [113].

stems from the fact that it is asymptotically equivalent to the Karhunen-Love transform which possesses optimal de-correlation as well as optimal energy compaction properties. Two-dimensinal wavelet transforms are well established in multimedia coding standards (H.265 and JPEG2000) [126]. Almost real-time hardware implementation is possible nowadays using dedicated Field Programmable Gate Array technologies, with 45 nanometer complementary metal-oxide-semiconductor (CMOS) standard cells capable of operating at 7.6 Gpixel/second for an 8x8 block rate at more than 100 MHz [127].

## 3.2. *Feature extraction methods*

Each T-ray measurement with $n$ data points can be viewed as a vector in a $n$ dimensional space, known as a *pattern space*. The time sequence then appears as a point in the pattern space. The object of feature extraction is to reduce dimensionality by converting pre-processed data to feature vectors. There are three considerations in the feature extraction and selection process: (i) the establishment of sound feature evaluation criteria, (ii) deciding the dimensionality of the feature space, and (iii) the choice of the algorithmic optimisation procedure adopted.

This analysis is carried out pixel by pixel, on the THz image. These feature vectors are grouped together via a decision function and then are evaluated to see whether they provide meaningful information. The features of interest upon which a classifier may be constructed are pulse height, shape, delays in the time domain, as well as the spectral content of the pulse in the frequency domain (after retaining both real and complex parts). Alternative parameters include the complex reflection coefficient commonly associated with an impedance mismatch and the complex insertion loss, commonly associated with the number of absorbers and extinction coefficient of the components in the sample. Differential transmittance and absorbance, with reference to a known sample can also provide contrast information which may be used for classification purposes.
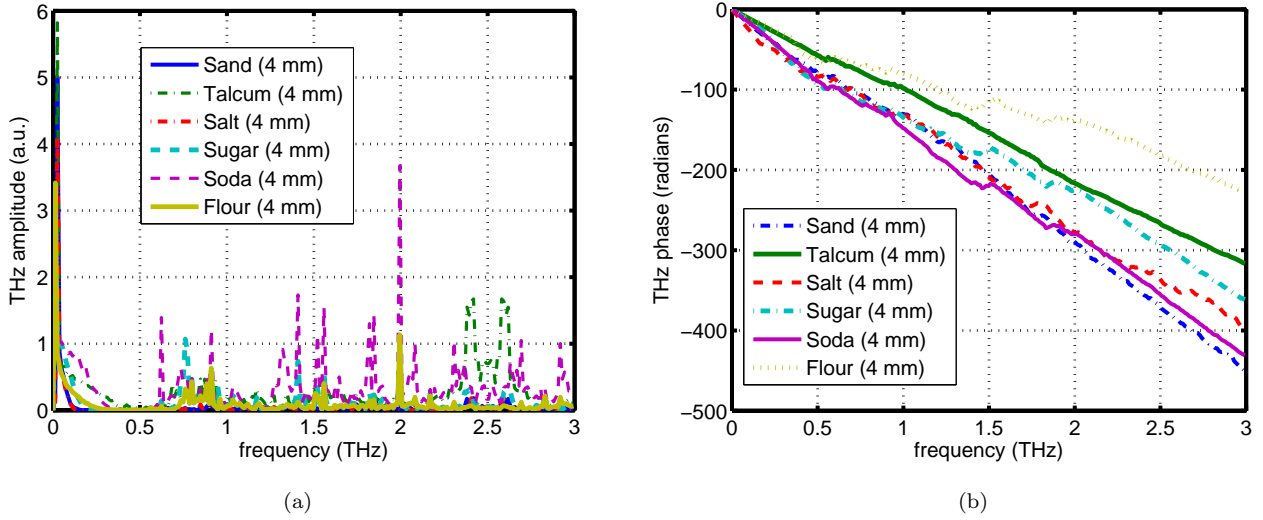
Fig. 7. Illustration of Fourier spectrum. (a) shows the amplitude (attenuation) as a function of terahertz frequency, whereas (b) shows the corresponding frequency dependent phase delay (equivalent to chromatic dispersion)

Essentially, features should consist of parameters that display non-transformed structural characteristics: moments, power, amplitude information, energy, etc. as well as transformed structural characteristics: frequency and amplitude spectra, coefficients from wavelet decomposition, AR, ARMA coefficients, coefficients derived using subspace identification methods from state space analysis of the corresponding time series, etc.

Pre-processing techniques focusing on dimensionality reduction in the feature space are at the core of a successful pattern recognition system. Inclusion of more features improves classifier performance but compromise the generalization ability of the classifier. This is the well-known curse of dimensionality [128], which becomes quite prominent if the number of features is above 30.

The fast wavelet transform may be adopted to achieve effective feature extraction. The features presented to the classifier, in this case become the extracted wavelet coefficients. The use of Auto Regressive (AR) and Auto Regressive Moving Average (ARMA) models on the wavelet transforms of measured T-ray pulse data has been previously discussed in our research paper [99]. The features of a processed THz signal are eventually classified by an Mahalanobis distance classifier. The effectiveness of this method is demonstrated via cancer cell discrimination from normal tissue and on the problem of recognising different kinds of powders.

### 3.2.1. Linear transforms for feature extraction

Linear transforms are useful both for noise extraction and for representing the information in the data using fewer coefficients. Noise extraction can be performed by assuming that the system is detector noise limited rather than source noise limited. In this case, the noise spreads equally among all transform coefficients, while useful information will generally be concentrated in a few coefficients. Examples of commonly used linear transformations for the processing of spectroscopic data include Fourier transform, windowed Fourier transforms, wavelet transforms, and principal-component analysis (PCA). A comprehensive evaluation of various linear transforms that may be used for the de-noising of spectra from continuous wave THz spectrometers can be found in [66], the main conclusions of the work are shown in Table 1.

**An example of using patterns in the spectra to perform classification of TPI signals is discussed in Yin et al. [129]. The amplitude and phase at certain key frequency components constitute pairs of feature subsets on which the classification is based. An important advantage of this approach is the small dimensionality of feature vectors. This allows the features to be directly extracted from pulsed responses with relatively low computational complexity. Fig. 7 shows the phase and amplitude plots in the frequency domain for six different powder samples: sand, talcum, salt, powdered sugar, wheat flour, and baking soda. Each curve is associated with a single pixel sampled from the image data. The spectrum has a cut-off frequency at 3 THz. Sharp changes of amplitude at the second frequency bin may be observed in Fig. 7(a). It can also be seen that samples have significantly different frequency dependent phase patterns, so that a classifier using this information can be implemented illustrated in Fig. 7(b). Please revise this paragrahy, suggested by our first reviewer.**

An example of using patterns in the spectra to perform classification of TPI signals is discussed in Yin et al. [129]. The amplitude and phase at certain key frequency components constitute pairs of feature subsets on which the classi-

Table 1
Advantages and Drawbacks of Linear Transforms

| Transform | Advantages | Disadvantages |
| --- | --- | --- |
| PCA:Y=U $\Delta$ $V^T$ | Maximum information compression | Each PC is related to the whole spectrum. "Problematic" regions in the spectrum cannot be excluded after the computation of the PCs. Since the analysis functions are obtained from the statistics of the data, many calibration samples may be required to obtain reliable PCs. |
| Fourier | The analysis functions are fixed. | Spatial information is lost. Problematic regions in the spectrum cannot be excluded after the transform. |
| Wavelet | Spatial information is kept. The width of the analysis window is automatically varied. | The choice of the mother wavelet is usually difficult. |

fication is based. An important advantage of this approach is the small dimensionality of feature vectors. This allows the features to be directly extracted from pulsed responses with relatively low computational complexity. Fig. 7 shows the phase and amplitude plots in the frequency domain for six different powder samples: sand, talcum, salt, powdered sugar, wheat flour, and baking soda. Each curve is associated with a single pixel sampled from the image data. The spectrum has a cut-off frequency at 3 THz. Sharp changes of amplitude at the second frequency bin may be observed in Fig. 7(a). It can also be seen that samples have significantly different frequency dependent phase patterns, so that a classifier using this information can be implemented illustrated in Fig. 7(b).

Zhang et al. [130] proposed two feature extraction methods to avoid misplacement phase error in terahertz reflection time-domain spectroscopy (THz-RTDS). In their work, the first or second order derivative of the phase of the relative sample reflectance was used to extract the frequency dependent absorption signatures of the materials under study. Ryniec et al. [131] applied decision trees as a feature selection method to identify terahertz spectra of different compounds, demonstrating the effectiveness of decision tree methods in the classification of THz spectra.

Generally, Fourier expansions suffer from drawbacks such as the notion of an infinite support in the time domain [25], which compromises the quality of the signal unless apodization routines are adopted [66] to eliminate Gibb's ripple resulting from discontinuities at the edges of the time domain interferogram. This is especially true when fast scan data acquisition is performed in TPI applications where the time domain signals are more truncated.

These drawbacks are more efficiently addressed through the use of windowed Fourier transforms that further reduce the number of coefficients needed to describe the transformed dataset in featureless parts of the spectrum as well as through the wavelet transform which addresses the issue by successively increasing the resolution (increase in scale) of both the temporal and frequency domain features of the TPI signal.

### 3.2.2. Wavelet coefficients as feature sets for THz pattern analysis

The objective of feature extraction techniques is to isolate the relevant features from the T-ray signals to improve classification performance. Wavelet transforms (WTs) complement the traditional Fourier-based techniques in THz signal analysis by providing superior time-frequency localization characteristics that are well-matched to the requirements for the short-duration T-ray pulse signals. Stephani *et al.* [132] used wavelet coefficients to extract features from hyperspectral THz-TDS datasets. The approach enabled a coarse pre-clustering operation representing the target images successfully. An alternative approach is through the wave atoms transform (WAT) which was first introduced by Fu et al. [133] in the context of THz transient processing of reflectance signatures. This is a multi-resolution technique that has a sparser expansion for oscillatory and oriented sample textures. It can provide improved resolution for pattern identification, when textural artefacts contaminate the THz transient response is concealing the compositional absorbance or reflectance of the sample.

An alternative to occasionally generate even more parsimonious feature matrices, reported by Yin et al. [99], assuming AR, MA and ARMA models of different order, may also be considered, depending on the data structure. In that approach, the averages of the modelling coefficients, (denoted as DC values in Fig. 7), are computed over the three decomposition levels of the wavelet transform employed on each data set. The model coefficient averages are then joined to produce feature vectors with a dimension equal to the number of sub-bands in the adopted wavelet decomposition. The feature vectors obtained from two different

AR orders, and MA orders may be combined respectively, to form the final AR and MA feature matrices. The AR-MA feature matrix is obtained by combining two different orders of AR and MA vectors together. The extracted AR and MA feature vectors are calculated at each decomposition level $j$. This approach may be introduced to further supress the number of features in the input of the classifier so as to further improve its generalization ability. The complete procedure for calculating $\mathbf{DC_j^{ARMA}}$ is depicted in Fig. 8.

An alternative to time-frequency analysis by wavelet transforms and further compression using MA routines is through the use of the Radon transform. Such approach has been used to successfully identify micro-Doppler motion of a target and has its origins in the high-resolution radar identification community. Xu et al. [134] suggested a combination of time frequency analysis with the Radon transform to perform micro-feature extraction but the approach incorporates echo-cancellation which often leads to an undesirable channel spectrum in the frequency domain, a common source of error in TPI imaging which can really compromise classifier performance. Alternative feature extraction procedures include principal components analysis (PCA), as discussed in [101] and [66]. The usual problem with such approach is the necessity to have a reliable set of calibration samples, which is often un-feasible.

### 3.3. *Pattern Classification*

In signal processing, pattern classification refers to the separation of patterns, measured or observed, into small classes, and then the assignment of each pattern to a particular class. The classification scheme is usually based on training sets that have already been successfully classified (supervised learning strategies). Learning can also be unsupervised, but such approaches fall usually away from a biomedical software certification perspective. The classification or description schemes that follow are mostly based on statistical (or decision-theoretic) approaches such as the Mahalanobis distance classifier, the Euclidean discrimination matrix, Support Vector Machines (SVMs) and Extreme Learning Machine (ELM) classifiers.

#### 3.3.1. *The Mahalanobis distance classifier via extracted features*

The Mahalanobis distance classifier [135] is a type of minimum distance classifier, which is optimal for normally distributed classes with equal covariance matrices (linear discriminant) and equal *a priori* probabilities. Such classifier is often chosen because it is simple to implement and it provides reasonable results for a variety of biomedical waveforms. One possible approach is to formulate the Mahalanobis classification scheme on a set of feature matrices of ARMA modelled datasets after signal decomposition in wavelet subbands [99]. For a given class, $m$, the distance from a feature matrix $\mathbf{DC_j^l}$ to the class mean $\mathcal{A}_m$, is defined as

$$\rho_m(X) = \sqrt{(\mathbf{DC_j^l} - \mathcal{A}_m)^{\mathrm{T}}\mathbf{C}_m^{-1}(\mathbf{DC_j^l} - \mathcal{A}_m)} \qquad (1)$$

where $\mathbf{C}_m$ is the covariance matrix of the feature vectors regarding class $m$, $\mathbf{DC_j^l}$ with $l = 1, 2, 3$ represents the averaged coefficients matrix related to AR ($l = 1$), MA ($l = 2$), and ARMA ($l = 3$) modeling of wavelet approximation coefficients at three decomposition levels $\mathbf{j}$, that is, $\mathbf{DC_j^1}$ being $\mathbf{DC_j^{AR}}$, $\mathbf{DC_j^2}$ being $\mathbf{DC_j^{MA}}$, $\mathbf{DC_j^3}$ being $\mathbf{DC_j^{ARMA}}$. In practice, the covariance matrix is estimated from the training vectors. During classification, the minimum Mahalanobis distance from feature matrix $\mathbf{DC_j^l}$ to each class centre $\mathcal{A}_m$ is used to assign the appropriate class label.

#### 3.3.2. *Support Vector Machine classifiers (SVMs)*

Kernel based learning and support vector machine (SVM) methodologies reside at the core of a range of interdisciplinary challenges. Their formulation shares concepts from different disciplines such as: linear algebra, mathematics, statistics, signal processing, systems and control theory, optimization, machine learning, pattern recognition, data mining and neural networks. The idea of the SVM is to map data from the input space into a high-dimensional feature space, in which an optimal separating hyper-plane that maximizes the boundary margin between two classes can be established. At its core, SVMs are two-class classifiers. In more recent times, SVMs have been extended to solve multi-class classification problems from noisy biomedical measurements. Furthermore, there are several reports discussing the use of SVMs for THz material identification. Pan et al. [136] used SVMs to classify THz absorption spectra for the purpose of illicit drugs identification. They successfully identified seven pure illicit drugs establishing the methodology as an efficient method for drug identification. Fitzgerald et al. [101] applied the SVM approaches combined with a radial basis function to discriminate normal from malignant breast tissue from THz-TPI. Yin et al. [129] applied SVMs to perform multi-class classification of THz powder spectra for six types of powder materials with similar optical properties. Fig. 9 illustrates the multi-class separation for the six types of powder substances using SVMs. SVMs are designed according to a pair wise-strategy. One real Gaussian kernel with $C = 1000$ and $\sigma = 1 \times e^{-7}$ is used to map the input data into a 2D Fourier feature space for visualisation purposes. The support vectors indicated by cyan circles are subsets of the training data sets and are used to construct a two-dimensional hyper-plane in feature space, which acts as a boundary separating each class of different powder materials.

#### 3.3.3. *Complex Valued ELMs for classification*

Our recent work [137] extended a very important class of recently developed classifiers called Extreme Learning Machines (ELMs) to complex valued problems [138, 139]. The motivation for the proposed extension stems from the
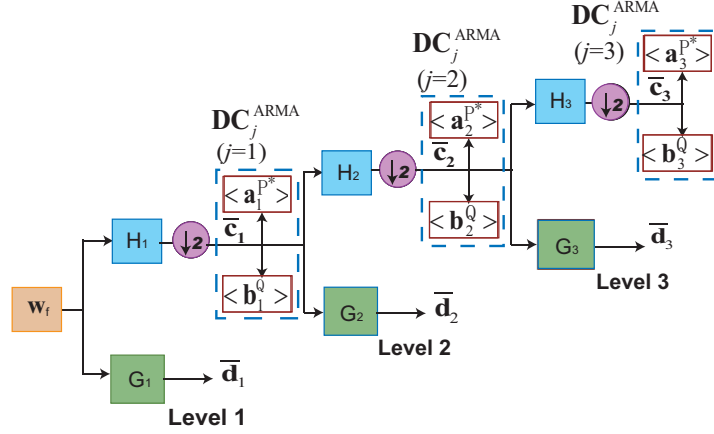
Fig. 8. In this modelling, $H$ and $G$ denote the low- and high-pass filters, respectively, $\mathbf{w}_f$ is the de-noised T-ray input. The arrow depicts the diadic down-sampling operator. Similar illustration related to $DC^{\mathrm{AR}}$ and $DC^{\mathrm{MA}}$ feature matrix are assumed.
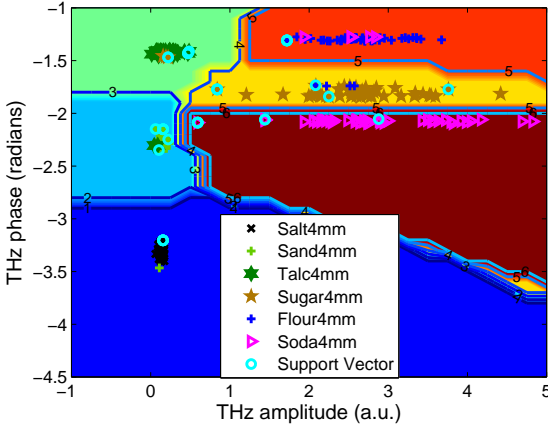


Fig. 9. Learning vectors for the powder data sets plotted to illustrate the linear decision function between the pairs of classes after applying a Gaussian kernel for mapping. There are 49 pixels selected randomly from each of the six powder samples. Background colour shows clearly the contour shape of the decision surface. The small yellow region on the bottom of the right hand side denotes undecided classification.

fact that the real valued ELM has shown some of the lowest training errors among machine learning algorithms and in particular support vector machines classifiers (SVMs) [25, 129, 140, 141]. Furthermore, existing machine learning techniques are focused on real valued datasets. Traditional amplitude only based pattern mining approaches of spatiotemporal images has classification limitations in highly correlated time-space features. CELM adopts induced complex RKHS kernels [142] to map inputs from complex-valued non-linear spaces to other real valued higher dimensional linear spaces. This permits us to classify the inputs with linear complex valued feature vectors. It involves aspects of quaternary classification, through the introduction of two complex-coupled hyper-planes [143]. A widely linear estimation processing approach is adopted and the argument composed of the sum of the two parts (real and imaginary)

is employed to model the output weights connecting the hidden layer with the feature mapping of the input into the hidden-layer feature space. The approach enables us to define a kernel function specific for the separation of the data in high dimensional complex coupled hyper-planes. The approach is compatible with the processing of datasets in tensorial format which enable additional image features (hyperspectral, amplitude, phase, polarization or spatiotemporal components) to be simultaneously retained.

The CELM classifier approach has a very broad applications domain across the biomedical community encompassing all types of research associated to the study of the interaction of matter with waves, and in particular spectroscopy (acoustic, dielectric, optical, terahertz, infrared, electronspin resonance, nuclear magnetic or paramagnetic resonance, etc.) as well as imaging and tomography modalities encountered across the Physical, Chemical and Biomedical disciplines. It is thus fundamental both from a Machine Learning as well as from a Chemometrics perspective [144]. Because the above relations are also analogous to the blurring function (relating amplitude and phase) developed by Bode [145] to describe the dynamics of physical systems, CELMs have a wide range of applications across all physical sciences. A typical example of the proposed approach is the recent study [146] which focused on the use of CELM to perform binary and multi-class classification of RNA and powder samples respectively on the basis of images acquired by THz-TPI. The analysis was performed on large data sets as would be the case in a typical bio-medical or quality control setting. Classification was performed on the basis of discernible features in the measured THz spectra. Examples of learning vector patterns for multiclass recognition via CELM, are shown in Fig. 10(a) after Fourier transformation of the time-domain signatures and extraction of the corresponding complex valued features in frequency domain, regarding phase and amplitude. We used 49 input vectors related to each powder sample for train-

15

ing the classifier. Two real RKHS kernels were used for mapping. The optimal Gaussian parameter of $\sigma$ was set to 100 and the penalty parameter $C$ was set to 0.1. The labels were complex-valued and produced 12 output classes. Background colour shows the contour shape of the decision surface, (these are numbered from 2–12), these correspond to the amplitude calculations derived from the sum of real and imaginary values of the respective complex labels. It can be observed that THz measurements of powder samples of salt, sand, talcum, are grouped more tightly than the powder samples of flour, soda and sugar. The labelled contours that correspond to different real and imaginary parts (the real and imaginary parts label the different classes) are illustrated in Fig. 10(b). These regions are undecided in the classification process and are therefore excluded to avoid over-fitting problems.

Complex valued extreme learning machine algorithms (CELMs) may be naturally extended to multi-pixel or voxel images. This aims to achieve complex valued learning of 3D inputs of complex valued features, i.e., to classify the complex valued input data selected from a tensor. The proposed approach will address aspects of quaternary classification within a tensor algebra context. For 3D inputs, three pairs of complex coupled hyperplanes will be designed through orthogonal projections. The approach enables us to define kernel function specific for the calculation of high dimensional complex coupled hyper-planes. It will allow effective classification of a more natural representation of the data in a tensor format.

### 3.4. *A further example for cancer diagnosis using THz imaging and pattern classification algorithms*

Eadie *et al.* [147] carried out multi-dimensional terahertz imaging analysis for colon cancer diagnosis. Their research uses decision trees to find important parameters, with neural networks and support vector machines that are used to classify the terahertz data as indicating normal or abnormal samples. This work finds the sensitivities of $90 - 100\%$ and the specificities of $86 - 90\%$ in the colon cancer diagnosis. Thus, the use of terahertz reflection imaging allows the colon cancer samples to be detected via optimized analysis of terahertz imaging data. The definitions regarding specification and specification can refer to Table 2.

### 3.5. *Clustering techniques to segment terahertz images*

Clustering, also termed cluster analysis is the formal study of algorithms and methods for grouping unlabelled data into subsets (called clusters) according to measured or perceived intrinsic characteristics or similarity. Clustering deals with data without using category labels that tag objects with prior identifiers, i.e., class labels. The absence of category information distinguishes data clustering (unsupervised learning) from classification or discriminant analysis (supervised learning). The two most frequently used clustering techniques are the K-means and the ISODATA clustering algorithm. Both of these algorithms are iterative procedures. In general, both of them assign first an arbitrary initial cluster vector. Then each pixel is classified to the closest cluster. Finally the new cluster mean vectors are calculated based on all the pixels in one cluster. The second and third steps are repeated until the "change" between the iteration is small. The "change" can be defined in several different ways, either by measuring the distances that the mean cluster vector have changed from one iteration to another or by the percentage of pixels that have changed between iterations. The ISODATA algorithm has some further refinements by splitting and merging of clusters [148]. Clusters are merged if either the number of members (pixel) in a cluster is less than a certain threshold or if the centers of two clusters are closer than a certain threshold. Clusters are split into two different clusters if the cluster standard deviation exceeds a predefined value and the number of members (pixels) is twice the threshold for the minimum number of members.

Currently, there are several papers report clustering techniques to segment terahertz images. Brun et al. [149] report on terahertz (THz) time-domain spectroscopy imaging of 10 $\mu m$ thick histological sections, where clustering methods is used to cluster THz spectral images that are produced through the extracted refractive index data. The results show that THz spectral differences exists not only between tumor and healthy tissues but also within tumors. Ayech and Ziou have produced a couple of research papers on K-means clustering methods for segmentation of terahertz imaging. In [150], a combination of autoregressive (AR) model and principal component analysis (PCA) is proposed to extract effective temporal/spectral features from THz pulsed images before carrying out soft decision of Kharmonic-means (KHM), which outperform the hard decision of traditional K-means. In [151, 152], a novel approach of segmentation of terahertz images is proposed, where the k-means technique is reformulated under a ranked set sample. Their approach consists to estimate the expected centers, select the relevant features and their scores, and classify the observed pixels of THz images. This method is essentially less sensitive to the initialization of the centers. A more recent research represented in [153] uses two-step partitional clustering approach to segment THz measurements of the inner structure of cave bear teeth. A k-nearest neighbor graph that is built on the reduced channel information [154] is further split into segments by a minimum edge cut bi-sectioning method. The results show that the layer-like structures are discernable within the material, giving a more detailed image of the inner structure of the tooth. Using ISODATA algorithm to cluster THz spectrum for THz image segmentation was first investigated by Berry et al. [155]. In their work, two specimens were examined in this pilot study, one of basal cell carcinoma and one of melanoma. Unsupervised ISODATA classification using three selected parametric terahertz pulsed images was compared qualitatively with k-means classification using the
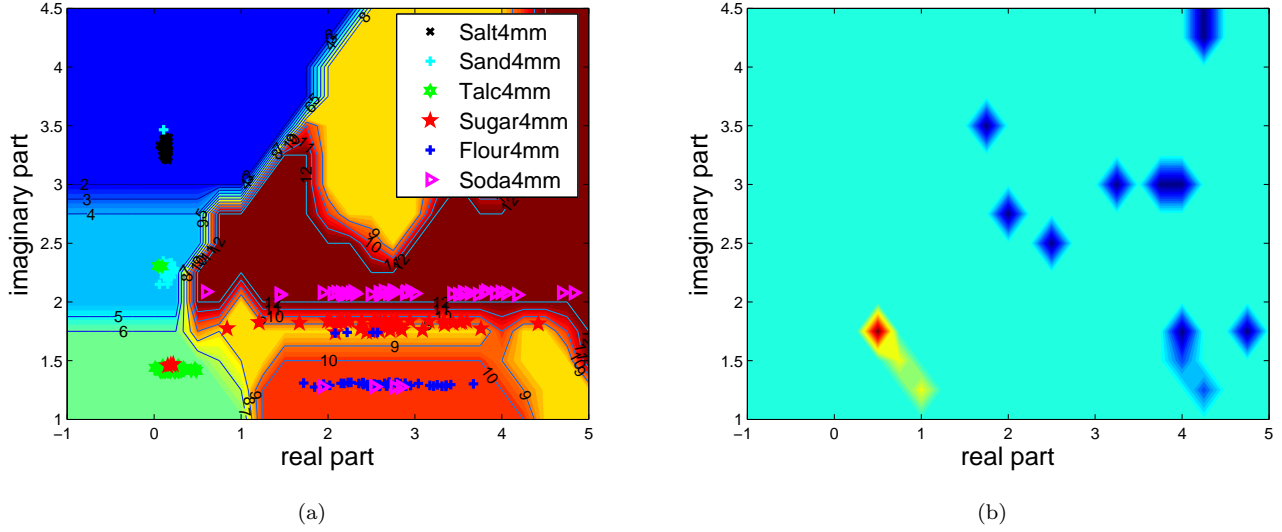
Fig. 10. Illustration of CELM multi-class classification scheme. (a) Complex valued learning vectors for the six samples plotted to illustrate the linear decision function among each classes by applying induced real RKHS kernels to map the complex input data into 2D complex valued feature space. There are 49 pixels selected randomly from each of the six powder samples. The labels are complex valued, generating 12 classes. (b) Illustration of the colour coded regions with non-zeros indicated by the colour bar. The colour regions with non-zero value indicate that the multi-class powder sample classification process remains undecided by CELM as the real and imaginary parts are not equal to each other.

shape of the whole time series, and with conventional s-tained microscope slides. There was good qualitative agreement between the classifications. Classifications were consistent with the morphological appearances expected. The results have implications for the future development of the technique as the need for only a small number of features could lead to considerably reduced acquisition times.

## 4. Analysis of DCE-MRI data

There has been already a decade since DCE-MRI was reported as a highly sensitive method for the detection of invasive breast cancer [156]. Because of its high 3D resolution and its ability to acquire kinetic contrast information, it has steadily gaining popularity over traditional diagnostic techniques such as mammography or ultrasound [157]. For breast tumors, lesion diagnostic sensitivities can reach 97% [158].

However, specificity of breast DCE-MRI is still rather low, with rates of between 30% and 70% [159, 160]. High false positive detection rates on MRI often lead not only to anxiety for the patient but may also result in an unnecessary invasive biopsy [157, 159]. This hinders its use as a routine imaging technique in breast cancer patients. Benefits of breast MRI include better cancer detection rates in high-risk women and providing more information regarding the extent of disease in women with known breast cancer.

Computer-aided diagnosis (CAD) approaches for breast MRI are typically employed for automatically identifying tumors from normal tissues when these are at a stage of rapid development [8, 13, 161, 162] whereas the more com-

plex task of classifying a lesion as benign or malignant [4, 20, 161, 163–170] is proving more difficult to address. In clinical practice, in order to enable the interpretation of patterns resulting from contrast enhancement across a series of MRI volumes, the intensity changes per voxel are color-coded by an automated kinetic assessment protocol. However, the technique is not fully automated and requires continuous feedback from experts. A major challenge in the diagnosis of breast DCE-MRI is the spatiotemporal association of tumour enhancement patterns, a task that humans are not as optimized to perform [4]. With many CAD systems now available commercially, Pan *et al.* [171] evaluate which system can best help detect signs of breast cancer on breast MRI. The most commonly used CAD systems in the USA are CADstream (CS) (Merge Healthcare Inc., Chicago, IL) and DynaCAD for Breast (DC) (Invivo, Gainesville, FL). Their primary objective in this study was to compare the CS and DC breast MRI CAD systems for diagnostic accuracy and postprocessed image quality. The experiments were to evaluate 177 lesions in 175 consecutive patients who underwent second-look ultrasound guided biopsy or MRI-guided biopsy. The results illustrate that the two CAD systems had similar sensitivity and specificity (CS had 70 % sensitivity and 32 % specificity whereas DC had 81 % sensitivity and 34 % specificity). Both CS and DC had a high sensitivity for detecting malignant lesions on breast MRI; however, neither system significantly improved specificity for the diagnosis of benign lesions. The ROC curve plots using both CS and DC systems are illustrated in Fig. 11.
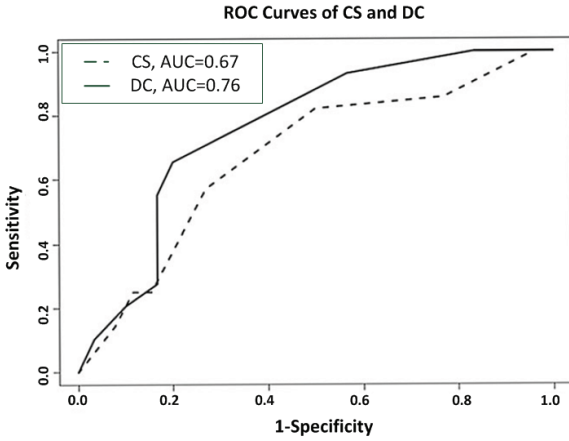
**ROC Curves of CS and DC**

Fig. 11. ROC curves of the mean scores for the CADstream and the DynaCAD for Breast systems. The figure shows the ROC curves based on the two mean diagnostic scores of the three raters for each software system. CS CADstream, DC DynaCAD for Breast, AUC area under the curve, ROC receiver operating characteristic. After [171].

### 4.1. *Outlook for future tensorial and Clifford algebra based feature and image registration*

In dynamic pattern recognition methods for the analysis of DCE-MRI, the emphasis has been on either high temporal resolution and empirical analysis [94, 172] or on high spatial resolution with a stand-alone morphologic feature extraction [172, 173]. Time-series analysis is a time-consuming task due to spatiotemporal lesion variability, and changes in spatial intensity of imaged tumours are other problems that cause an inherent difficulty in segmentation of an object of interest [174]. For example, Fig. 12(a) depicts an imaged ductal carcinoma in situ (DCIS). While the parts depicted by the arrows show the same anatomical structure taken from the same tumour region, the intensity values are different. The intensity indicated by a yellow arrow is higher than the intensity indicated by the red arrows. After conducting intensity based segmentation as illustrated in Fig. 12(b), the region with low intensity may feature as a gap separating the image into two disconnected parts. The gap forms an area without edge. A multi-channel classification method that consider the associations between spatial and temporal features of high-dimensional images is proposed in order to achieve accurate diagnosis of tumour tissues. The detection of anomalies in spatiotemporal data is an emergent interdisciplinary topic that involves highly innovative computer science methods. Mining spatiotemporal patterns is critical for the correct identification of tumour anomalies in DCE-MRI and yet remains challenging because of complexities in analyzing the time-series of three-dimensional image data.

Tensor decomposition of high-dimensional medical image data, i.e. fMRI, has gradually drawn attention since it can explore the multi-way data's structure which exists inherently in human organic imaging [175]. Tensors are mul-

timode (multi-way) arrays, of whom vectors (i.e., one-mode tensors) and matrices (i.e., two-mode tensors) are special cases. The tensor representation captures useful information that is difficult to provide in a conventional vectorial formalism. To effectively utilize the rich information contained in tensors, we propose to extend the CELM for effective tensor classification. Since most standard learning algorithms assume data instances are feature vectors, it is not straightforward to apply these algorithms on tensorial data. The CELM method enables the identification and learning of inter-mode relations of features.

Unlike classic SVMs, the complex valued hyper-planes of CELM are addressed via calculating the smallest norm of output weights with the smallest training error in a similar manner as in ELM, which discards the normal threshold found in SVMs, without calculating support vectors. The extended CELM has significant potential to solve complex valued problems for multiclass classification of tensorial datasets with dramatically reduced computational complexity and significantly improved computational speed. It enables the classification of tensorial data while preserving information associated with adjacent and overlapping data vectors as well as differentially extracted features.

Registration of images is a crucial step in many image processing applications where the final information is obtained by combining multiple input images. In many applications multi-channel images are available, which require adequate processing of vector data. However, traditional approaches in achieving multi-channel image registration can cause inaccuracies by introducing information loss or misinterpretations and may lead to inappropriate results. An alternative way to perform registration of multichannel images described by associated vectorial datasets is through the use of Geometric Algebras (such as Clifford Algebra). The main advantage of this algorithm is that it directly operates on the multichannel signal, instead of scaling the signal down to one dimension (e.g. by averaging) and thereby loosing a lot of information.

### 4.2. *Performance measures*

Evaluation of diagnostic tests is a matter of concern in modern medicine not only for confirming the presence of disease but also to rule out the disease in healthy subjects. The diseased subject detection process via DCE-MRI aims to achieve voxel-based classification result. From the frequency of test results among patients with and without disease based on gold standard, any voxel in MRIs can be classified either as diseased or surrounding tissue. Consequently, there are four possibilities; two classifications and two misclassifications. The classifications are the true positive (TP) and the true negative (TN) where the number of tumour voxels and background voxels which are correctly detected respectively; the false positive (FP) is the number of pixels not belonging to a vessel, but is recognised as one, and the false negative (FN) is the number of pixels be-
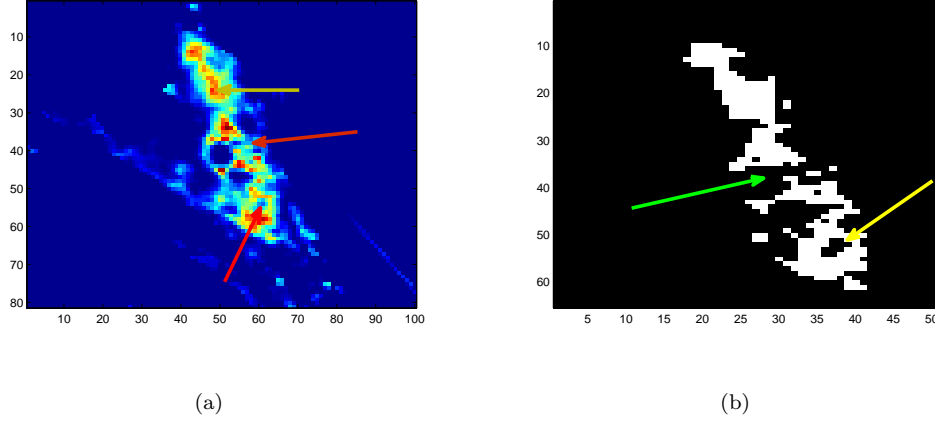
Fig. 12. (a) illustration of intensity inconsistency for breast tumour tissue images. Yellow arrows indicate a high intensity and red arrows low intensity. (b) Illustration of intensity based segmentation with inhomogeneous boundaries; yellow arrows indicate an irregular ring region with hole inside and a green arrow indicates missing areas.

longing to a vessel, but is recognised as background pixels, mistakenly.

One can further derive the probability of a positive test result for patients with disease and the probability of negative test results for patients without disease. The true positive rate (TPR) represents the fraction of voxels correctly detected as diseased voxels. The false positive rate (FPR) is the fraction of voxels erroneously detected as diseased voxels. The accuracy (Acc) is measured by the ratio of the total number of correctly classified voxels (sum of true positives and true negatives) to the number of voxels in the image field of view. Sensitivity (SN) reflects the ability of the algorithm to detect the diseased voxels. Specificity (SP) is the ability to detect non-diseased voxels. It can be expressed as 1-FPR. The positive predictive value (PPV) gives the proportion of identified diseased voxels which are true diseased voxels. The PPV is the probability that an identified diseased voxel is a true positive.

A receiver operating characteristic (ROC) analysis has become a popular method for evaluating the accuracy of medical diagnostic systems. ROC curve plots the fraction of diseased voxels correctly classified as diseased tissues, namely the TPR), versus the fraction of non-diseased voxels wrongly classified as diseased voxels, namely the FPR). The better performance of the system is closer to the upper left hand corner of the ROC space. The most frequently used performance measure extracted from the ROC curve is the value of the area under the curve (AUC) which is 1 for an optimal system. For MRI images, the TPR and FPR are computed considering only voxels inside the FOV. Table 2 summaries the performance metrics used by DCE-MRI image segmentation algorithms.

Table 2
Performance metrics for diseased tissue detection process via DCE-MRIs

| Measure | Description |
| --- | --- |
| TPR | TP/deased voxel count |
| FPR | |
| FP/non-diseased voxel count Specificity | TN/(TN + FP) |
| Sensitivity | TP/(TP + FN) |
| Accuracy (Acc) | (TP +TN)/FOV voxel count |

### 4.3. *Extensions to multi-channel classifiers*

Using tensor algebra can assist analysis of spatiotemporal associated features and will allow development of a multidimensional unified MRI framework for processing DCE-MRIs. Mining spatiotemporal associated features of lesions from MRIs can increase the accuracy and efficiency of pattern identification. Current DCE-MRI is not sufficiently accurate for the early detection of tumours because of a lack of association between the spatial and temporal features.

In this section, we introduce a novel dynamic tensor reconstruction algorithm aimed at principal component separation. This is addressed via an offline tensor analysis algorithm (OTA) in combination with PCA. It focuses on the analysis of dynamic projection matrices for principal component separation of cancerous and healthy tissues.

**Figure 10(a)-(e) provides an illustration of the differentiation between the fourth post-contrast enhanced images and base line images from layer 71 to layer 75. (a)-(e) Illustration of the differentiation between the fourth post-contrast enhanced images and base line images from layer 71 to layer 75. Plsease revise this paragraph as suggested by our first reviewer.** (f)-(j) Illustration of the images achieved

by applying the proposed tensor reconstruction algorithm on six subtracted images with different time frames, one of which is illustrated in (a)-(e). (k)-(o) Illustration of the extracted volume image in relation to tumor region via applying FCM on the reconstructed images shown in (f)-(j). The tensorisation of DCE-MRI is reconstructed via multidimensional unified analysis of MRI data according to tensor factorization. One of the advantages of such a reconstruction is to blend the temporal information into spatial voxels and projecting four dimensional time-spatial vectors into a three dimensional space that shows spatial and temporal information fusion with decreased number of dimensions for reduced computation cost.

### 4.4. *Image registration of DCE-MRIs*

In DCE-MRI, there are (i) spatial motion artefacts caused by patient movement, respiratory motion, intestinal peristalsis and cardiac pulsations during data collection [176–178], and (ii) signal intensity changes in T1-weighted images when the contrast agent diffuses out from the vascular tissue and accumulates in the interstitial space. These signal intensity variations lead to contrast agent concentration estimation errors which can further amplify errors in pharmacokinetic models of tissue blood volume and vascular permeability compromising evaluations of therapeutic response [179]. Proper registration of pixels in the chosen co-ordinate frame is a critical step in the data acquisition process as uncorrected voxel displacements from the motion artefacts will corrupt the voxel information.

In DCE-MRI data, there are also further challenges as time progresses after compound injection. Both rigid (alignment using only translation and rotation) and non-rigid algorithms (associated with more complex deformations) have been proposed for image registration, i.e. in DCE-MRIs of kidney [180], breast [181], liver [182], lungs [183, 184] and the heart [185]. Reviews discussing advances in DCE-MRI image registration can be found in [176, 186, 187]. A conceptually straightforward rigid transformation is through manual delineation of the volume images of the target object after aligning the centers of gravity [188]. An automated feature-based algorithm has been presented by Song et al. [189]. In this work, wavelet-based edge detection is followed by the computation of a geometric transformation based on a Fourier transform. Zikic et al. proposed a locally rigid registration algorithm with a gradient-based similarity measure to allow for global changes in kidney enhancement [180]. Another approach is to register the images by optimizing the fit of the enhancement curves to a pharmacokinetic model [190] and [191]. Nonrigid algorithms include a vertical, deformable transformation minimizing a cost function which suppresses motion and smoothes the enhancement curves [192] while at the same time maximize the mutual information using a cubic B-splines deformation [181, 193]. More recent approaches to registration aim to incorporate additional a priori information based on specific anatomical markers [194], volume preservation of tissue [195] or local rigidity assumptions[196]. Schäfer *et al.* [197] propose a regional segmentation approach to study breast tissue lesions taking into consideration whether there was an observed similarity in the tissue perfusion characteristics, thus improving on single voxel-based approaches [198]. This approach has also additional advantages from a clinical diagnostics perspective.

Current literature [182] suggests that there are advantages in non-rigid registration when compared to rigid registration. For non-rigid registration, deformable image registration of DCE-MRI time series is accomplished using (normalized) mutual information (MI) [178, 199] approaches. Normally, the images contain edge information between various tissue types. A gradient dependent cost functional is proposed for registration. In recent work, it was shown that normalized gradient fields (NGF) provide a viable alternative to MI for the registration of DCE-MRI images [176].

An alternative approach to non-rigid motion correction uses a Bayesian framework [200] to provide pharmacokinetic parameter estimation in DCE-MRI sequences. A physiological image formation model is used to provide the similarity measure used for motion correction. Hodneland et al. [176] compared a normalized gradients approach with the mutual information approach for motion correction of DCE-MRI datasets and showed that using cost functions based on normalized gradients can successfully supress artefacts from moving organs in clinical DCE-MRI records.

An alternative approach, proposed by Lin et al. [201] discusses a respiratory motion-compensated DCE-MRI technique using k-space-weighted image contrast (KWIC) radial filtering. The technique combines the self-gating properties of radial imaging with the reconstruction flexibility provided by the golden-angle view-order strategy. The signal at the k-space center is used to determine the respiratory cycle, and consecutive views during the expiratory phase of each respiratory period are grouped into individual segments. The principle is to divide k-space into concentric rings. The boundary of each circular region is determined by the Nyquist criterion, after assuming that the views within each region have uniform azimuthal spacing.

The feature extraction algorithms mentioned earlier are relevant to both medical image registration as well as motion compensation [202, 203]. An alternative approach to localize anatomical features in DCE-MRI is using level sets, an approach originally proposed in [204, 205]. The method is applicable to post-contrast enhanced MR images to delineate the variable shape of features of interest. Yin et al. [206] proposed such approach to localize anatomical features in-breast costal cartilage imaged using DCE-MRI. The contours in each layer are cumulatively added to the first contour to produce the results illustrated in Fig. 14(a). The shape of the feature of interest clearly varies from layer to layer. The variable shape of contours acquired from a level-set-based segment image actually determines the feature region of interest. This is subsequently used as a guide
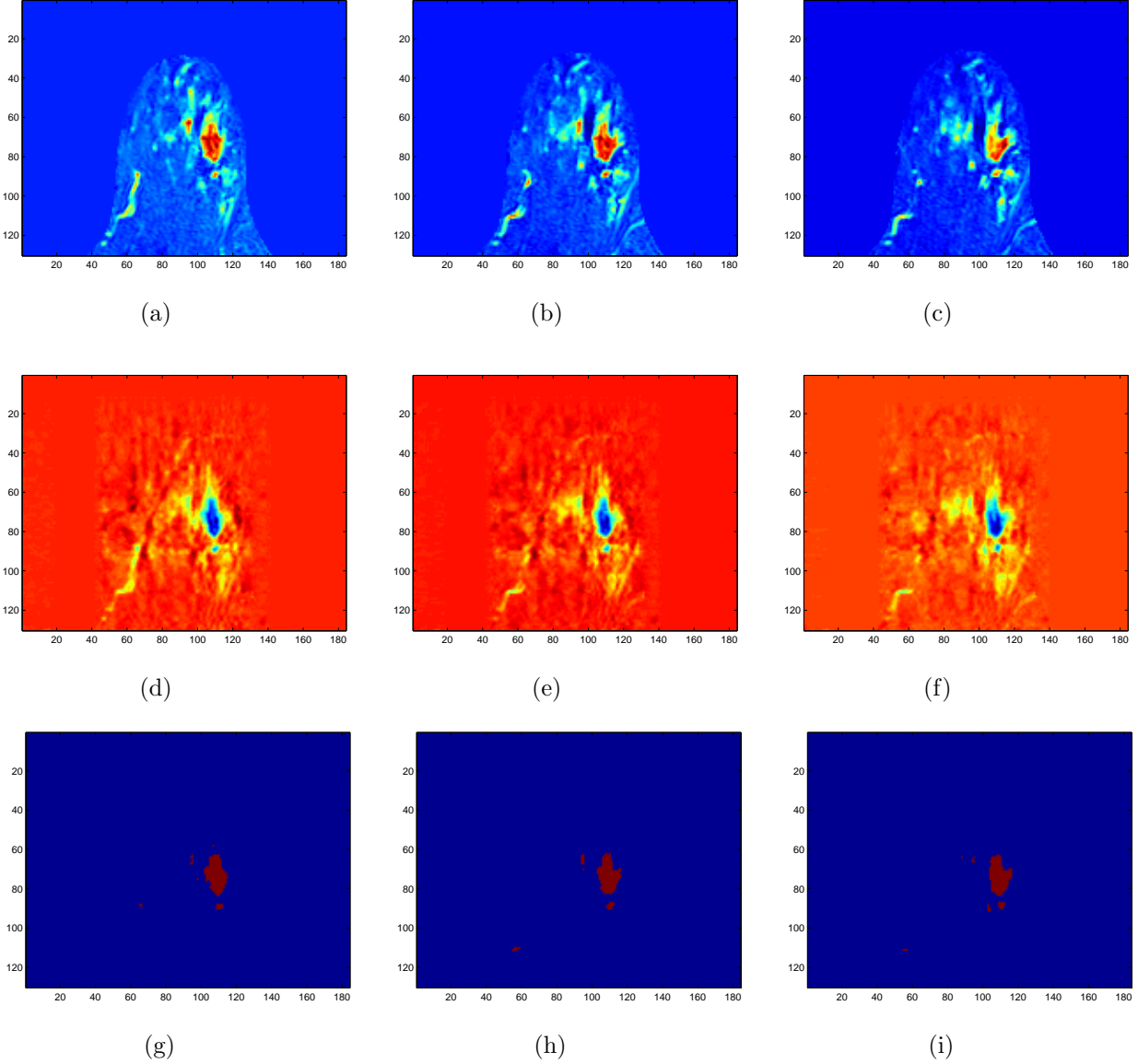
Fig. 13. Tensor reconstruction of preprocessed DCE-MRIs. (a)-(c) Illustration of the differentiation between the fourth post-contrast enhanced images and base line images from layer 71 to layer 75. (d)-(f) Illustration of the images achieved by applying the proposed tensor reconstruction algorithm on six subtracted images with different time frames, one of which is illustrated in (a)-(c). (g)-(i) Illustration of the extracted volume image in relation to tumor region via applying FCM on the reconstructed images shown in (d)-(f).

to specify initial masks for feature extraction. Fig. 14(b) shows the superposition of the mask and the level-set based projection of Fig. 14(a). The motion action of the fourth pair of breast costal cartilages are obtained by re-projecting the resultant segments from transaxial planes to sagittal planes. Rotational motion artefacts in the DCE-MRI are illustrated in Fig. 14(c).

### 4.5. Pattern identification of spatiotemporal association features of tumours in DCE-MRI data

One of the current challenges in breast DCE-MRI as a screening modality is reducing false positive detection errors, thereby boosting detection specificity. Computer-

aided diagnosis (CAD) approaches for breast MRI are typically employed for automatically identifying tumors from normal tissues when these are at a stage of rapid development [8, 13, 161, 162] whereas the more complex task of classifying a lesion as benign or malignant [4, 20, 161, 163–170] is proving more difficult to address. In dynamic pattern recognation methods, the emphasis has been on either high temporal resolution and empirical analyses [4, 17–20] or on high spatial resolution with a standalone morphologic feature extraction [4, 8, 9, 162, 167, 170]. Even though time-series analysis enables radiologists to infer information regarding the tissue state, such assessment is a time-consuming task, because of spatiotemporal lesion variability. Currently, most studies consider aggregate measurements for tumour morphological characterization
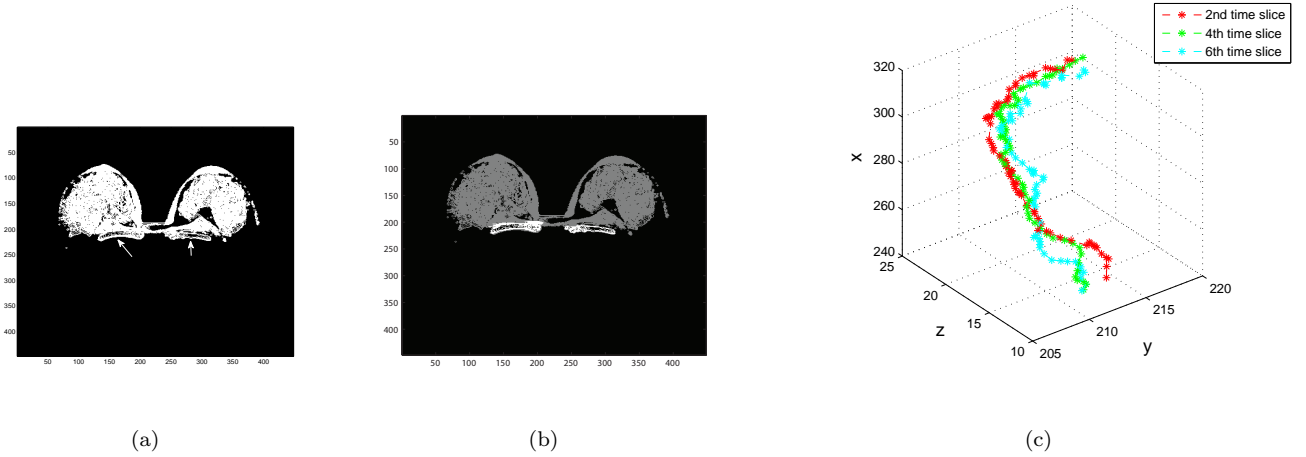
Fig. 14. (a) Cumulative contours from 25 layers' result from the level-set method, with two white arrows indicating the positions of features of interest. (b) Illustration of the superposition between the total segment and the level-set based segment. (c) Illustration of the 3D plots of plane centroid produced datasets.

[4, 162, 170] with an initially model-free [162, 170] and data-driven [13, 161] segmentation according to manually marked region-of-interest (ROI).

Common practice in these methods is to process the imaged 3D volumes separately, and then incorporate the temporal information into the spatial databases through a separate processing step. Image reduction based feature extraction enables identification on the basis of the dominant features present in the image. For example, in [14, 15], principal component analysis (PCA) was applied on enhanced and scaled datasets for a whole 2D object region obtained by DCE-MRIs. This is in contrast to traditional PCA applied in two-dimensional MRI image analysis ignoring any spatial information associated with a time series evolution of disease progression. To address the issues of low specificity and high inter-observer variability in breast DCE-MRI, the analysis of spatiotemporal patterns remains challenging [4] and requires the development of new software tools.

Representation of multi-dimensional features in a tensor space is a relatively new concept in the computer science and pattern recognition literature. The motivation of using tensor decomposition is to explore via multimode data analysis of image arrays the spatiotemporal correlations of sequences of DCE-MRI images. Recent work [207] shows that there is potential to identify tumour shape by combining non-negative tensor decomposition and directional texture synthesis. The approach uses symmetry information about 3D shapes that is represented by 2D textures synthesised from sparse, decomposed images.

Tensorial analysis is directional so interactions of components within the associated matrices provide additional degrees of freedom for data analysis, enabling spatiotemporal data correlations to be made along each co-ordinate direction as shown in Fig. 15(a). Isolation of such correlations in each co-ordinate plane can provide a clearer picture of dis-

ease proliferation. A third order tensor that may be associated with a DCE-MRI dataset is illustrated in Fig. 15(b)-(d). Fig. 15(e) illustrates the way to flatten the third order tensors along frontal slices.

Tensor factorisation of a 3D spatial matrix uses multilinear algebra to analyse an ensemble of volume images, in order to separate and parsimoniously represent high-dimensional spatial datasets into constituent factors [208]. The 3D spatial image datasets are treated as a third order tensor. The image dataset tensor $\mathcal{A}^{(3)} \in \mathbb{R}^{I_1 \times I_2 \times I_3}$ is decomposed [209] or factorised to a core tensor $\mathcal{C} \in \mathbb{R}^{J_1 \times J_2 \times J_3}$ and three different modes of 2D image matrices $\mathbf{X}^{(n)} \in \mathbb{R}^{I_n \times J_n}$, $n = 1, 2, 3$, as illustrated in Fig. 15(f).

In our recent research [207], we explored tensor decomposition for the identification of shape with mirror symmetry. We conclude that if both the first mode matrix (i.e. along the $y$ and the $z$ axes) and second mode matrix (i.e. along the $x$ and the $z$ axes) are symmetric, the frontal plane (along the $x$ and the $y$ axes) is a mirror symmetric plane, and vice versa.

Spatial shape datasets with a simple geometry is used for an illustration purposes. Fig. 16 illustrates the three-dimensional mirror symmetry analysis of a spherical object with a radius of 31 pixels. Fig. 16(a) illustrates that the flattened basis images are cropped in the middle area after non-negative tensor decomposition of the sphere. As an example, it is obtained via tensor multiplication of the core tensor, first mode and second mode matrices. Fig. 16(b) illustrates sparse texture extraction of the spherical object. Fig. 16(c) shows a synthesis of the extracted texture regarding the sphere. The resultant synthesised image is symmetric with both vertical and horizontal symmetric axes, which means the object is symmetric with the frontal plane as a reflective mirror.

A second case is to explore the mirror symmetry of brain

22
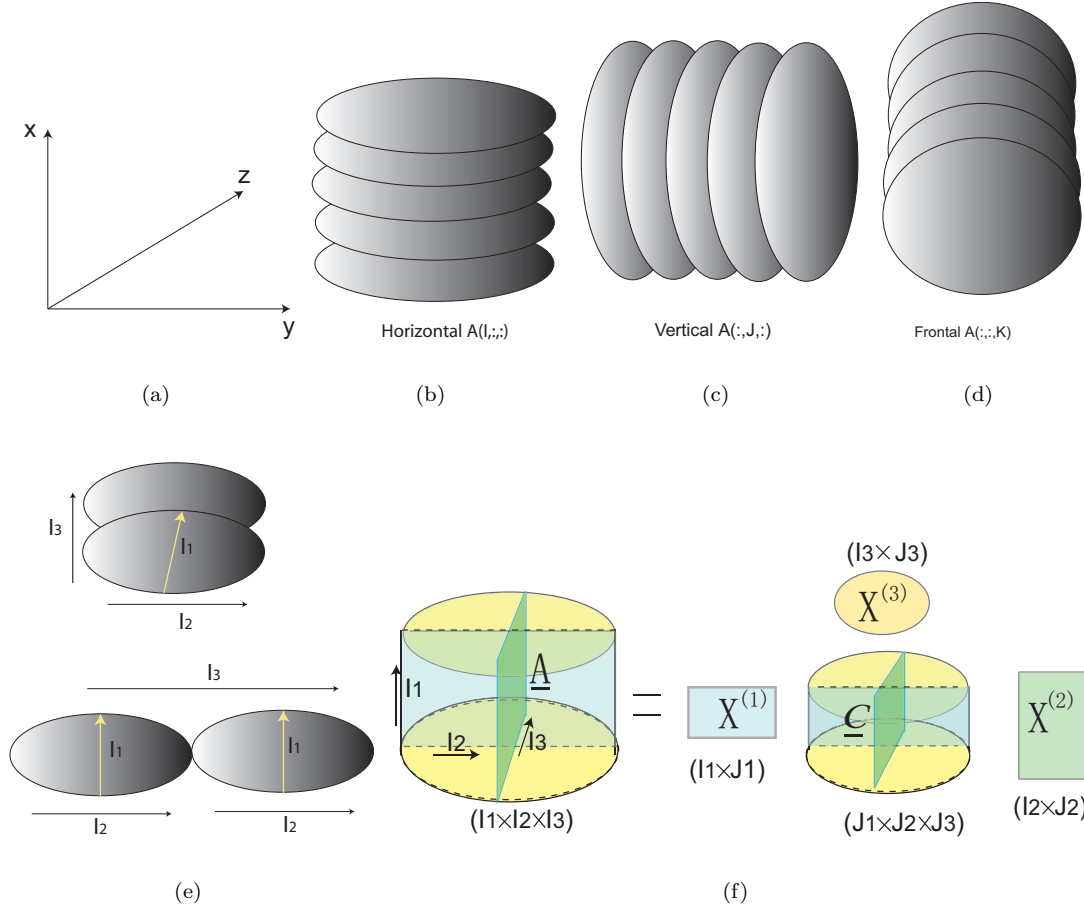
Fig. 15. (a) Illustration of the directions regarding the $x$-, $y$-, and $z$-axis. (b), (c), and (d). Illustration of three direction slices of a third order tensor: horizontal, vertical, and frontal, respectively, which are perpendicular to the $x$-, $y$-, and $z$-axis, respectively. (e) Illustration of the way to flatten the third order tensors along frontal slices. The colon (:) used in the figure indicates all the column elements at a given direction are involved to form an image matrix. (f) Illustration of a third-order decomposition.



Fig. 16. Illustration of three-dimensional mirror symmetry analysis of a spherical object. (a) Non-negative tensor decomposition. (b) Sparse texture extraction. (c) Synthesis of the extracted texture.

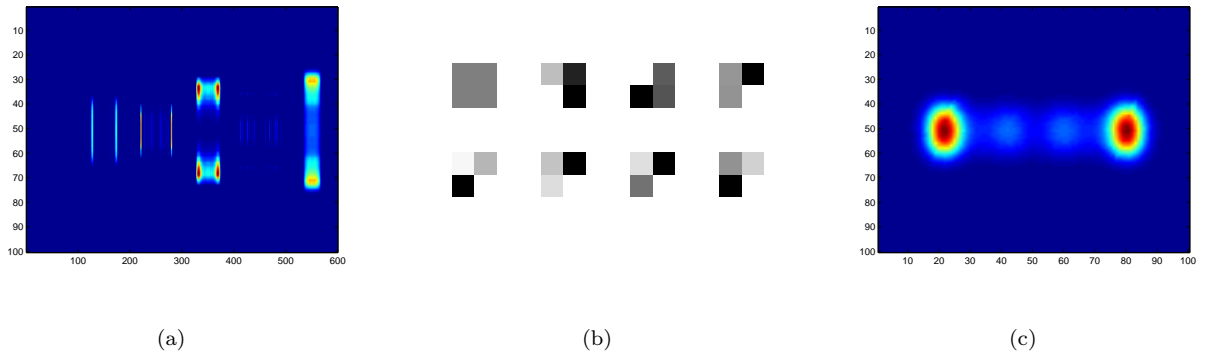structural MRI of white mass with rough resolution. The MR image size is $47 \times 58 \times 43$. Fig. 17 (a)-(c) illustrate one of the 2D cross-sectional slices along a horizontal plane, vertical plane, and frontal plane. Fig. 17 (d) illustrates a brain slice image with asymmetry along an $x$-$y$ plane.

The generated 3D images with symmetry and asymmetry are assembled into the third order tensors and non-negative tensor decomposition is applied to factorise the non-negative tensors to factors, with the core tensor size of $32 \times 32 \times 32$ and the flatten basis image size of $58 \times 1024$. The center region of the basis images is cropped to a size of $58 \times 180$. Fig. 18(a)-(d) illustrate the resultant synthesis for the symmetric MRI, and the generated the first (with 15 asymmetric layers), the second (with 25 asymmetric layers), and the third (with 35 asymmetric layers) asymmetric MR images.

To ascertain the degree symmetry (or the lack of it), (i) $k$ means clustering is used to group the synthesis patterns and find the associated 2-dimensional geometric pattern; (ii) histogram images from the synthesis patterns are used to evaluate the degree of intensity symmetry in the image. In this way, the analysis of 3D shape can be mapped into 2D space, therefore, performing the required dimensionality reduction. The current study thus proposes a way forward towards addressing the challenges associated with tensor decomposition of MRIs for abnormality detection of simulated breast tumours.

This is currently most relevant to MRI in clinical practice, but can benefit the TPI community, especially if such systems are to soon undergo further clinical trials.

## 5. Conclusion and future work

This work considered commonalities in datasets acquired using TPI and DCE-MRI measurement modalities. Both approaches are currently being explored as viable alternative imaging modalities to assess disease proliferation in a non-invasive manner. DCE-MRI is well established and as such it is regularly used in clinical environments. In contrast, TPI has yet to gain popularity although there is a general recognition of its potential to provide complementary information to clinicians.

TPI scans provide information from individual pixels that show wavelength dependent attenuation, dispersion and phase delay according to the state of hydration of the tissue. Specific vibrational signatures may also be identified in the frequency domain after Fourier transformation of the time-domain data. Similarly, MRI datasets are based on observations of de-excitation lifetimes so there are common grounds for the signal processing of both signal types. Furthermore, in both cases, specific signatures may be identified and assigned to biomarkers to improve on specificity and additional molecular identification of compounds.

Both systems have slow image acquisition rates. This can be distressing to patients in a clinical environment and leads to movement artefacts which need to be corrected. Correc-

tion algorithms using image registration can account for the movement of organs in DCE-MRI, but have yet to be used by the TPI community. Signal de-noising is more advanced in the THz community, whereas techniques for sparser data acquisition are more developed in the MRI community. There is therefore scope for placing these algorithms in a more unified framework. Both scanning systems generate very large datasets which need to be appropriately managed by trained professionals. In addition, both systems can be enhanced by pulse shaping methodologies that can selectively excite molecular systems. Pre-processing using adaptive signal apodization, can maximize the resolving power of the imaging system. The fitting of ARX, ARMAX and subspace identification models can provide a more parsimonious signal representation that can facilitate de-noising and extract de-excitation lifetimes in a very parsimonious manner. In TPI, wavelet de-noising, especially using adaptive wavelets can compress the signals to a few coefficients before introducing them into a classifier. SURE de-noising provides a universally accepted way to perform thresholding of coefficients associated to any of the above data transformations. Modelling using fractional order system identification routines is also an important emergent modality of relevance to both imaging systems.

To achieve accurate detection and diagnosis of tumours, emphasis should be placed on the analysis of spatiotemporal features using a unified perspective. Automatic classification may be performed using either Mahalanobis, SVM or ELM classifiers. In the case of SVM and ELM algorithms, their complex extensions are more useful because features in amplitude and phase or time and frequency respectively may be simultaneously presented to the classifier as different entities. Separately tuned kernels for the real and complex parts of the signal can improve classification accuracy. Extensions to multi-channel kernels using quaternary algebra and tensorial image registration enable additional measurement parameters to be considered such as state of polarization, or additional image morphological features such as tissue folds and striations that account for different degrees of dispersion of the signal in preferential directions across an image to be taken into consideration at the input space of the classifiers. Such approach can lead to improved classification accuracy. Multi-channel classifiers also enable information from other sensing modalities associated to image de-blurring to be taken into consideration in the classification task. Such approach also enables information from images at different time stamps to be also fused before being presented to the classifier.

The observed commonalities in the signal processing of both datasets demonstrate that it is natural to envisage future systems combining both diagnostic capabilities. There is thus a need to integrate the proposed algorithms under a single software environment for data analysis and visualization. Such approach will potentially lead to automated quantitative assessment of disease proliferation in a manner that may be accepted by clinicians.
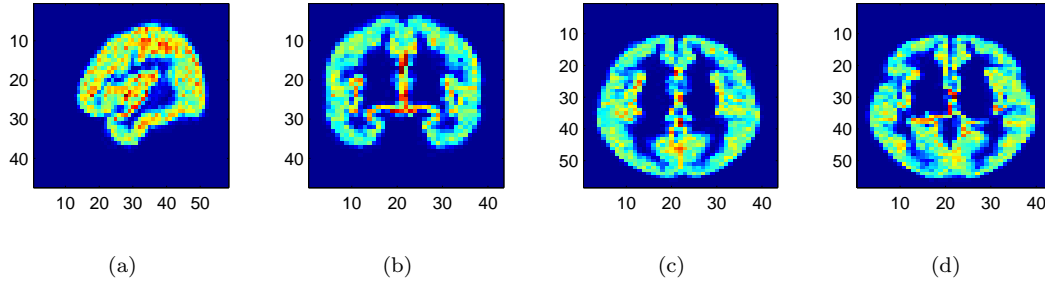
Fig. 17. Illustration of the mirror symmetry of brain structural MRI with rough resolution. The brain MRI size is $58 \times 47 \times 43$. (a)-(c) Illustration of 2D cross-sectional slices along a horizontal plane, vertical plane, and frontal plane. (d) Illustration of a brain slice image with asymmetry along an $x$-$y$ plane.
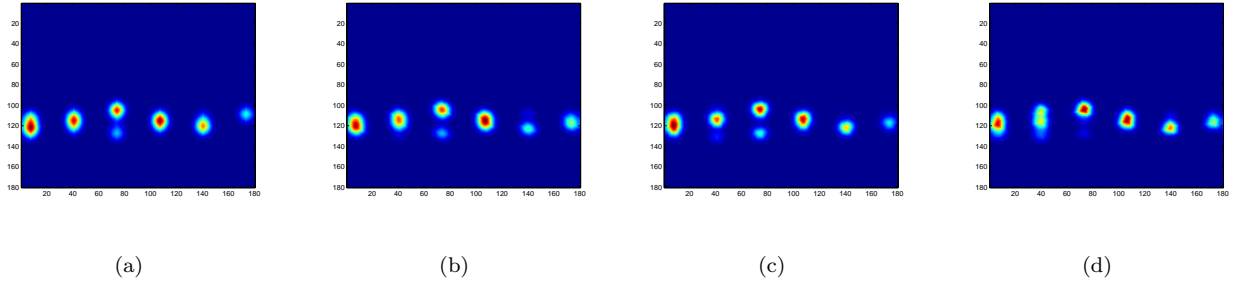


Fig. 18. Illustration of the synthesised images related to the generated 3D brain structural MR image with symmetry (refer to Fig. 17(a)-(c)) and asymmetry (refer to Fig. 17(a),(b), and (d)). (a)-(d) Illustration of the resultant synthesis for the symmetric brain structural MRI, and the generated the first (with 15 asymmetric layers), the second (with 25 asymmetric layers), and the third (with 35 asymmetric layers) asymmetric brain structural MR images, respectively.

## References

[1] H. Frölich, "The biological effects of microwaves and related questions," *Advanced Electronics Electron Physics* **53**, pp. 85–152, 1980.

[2] W. Grundler and F. Kaiser, "Experimental evidence for coherent excitations correlated with cell growth," *Nanobiology* **1**, pp. 163–176, 1992.

[3] A. Karahaliou, K. Vassiou, N. S. Arikidis, S. Skiadopoulos, T. Kanavou, and L. Costaridou, "Assessing heterogeneity of lesion enhancement kinetics in dynamic contrast enhanced MRI for breast cancer diagnosis," *The British Journal of Radiology* **83**(988), pp. 296–309, 2010.

[4] S. H. Lee, J. H. Kim, N. Cho, J. S. Park, Z. Yang, Y. S. Jung, and W. K. Moon, "Multilevel analysis of spatiotemporal association features for differentiation of tumor enhancement patterns in breast DCE-MRI," *Medical Physics* **37**(8), pp. 3940–3956, 2010.

[5] N. Bhooshan, M. L. Giger, S. A. Jansen, H. Li, L. Lan, and G. M. Newstead, "Cancerous breast lesions on dynamic contrast-enhanced MR images: computerized characterization for image-based prognostic markers," *Radiology* **254**(3), pp. 680–690, 2010.

[6] C. F. Beckmann and S. M. Smith, "Tensorial extensions of independent component analysis for multi-subject FMRI analysis," *Neuroimage* **25**(1), pp. 294–311, 2005.

[7] W. Chen, M. L. Giger, L. Lan, and U. Bick, "Computerized interpretation of breast MRI: investigation of enhancement-variance dynamics," *Medical Physics* **31**(5), pp. 1076–1082, 2004.

[8] Y. Zheng, S. Englander, S. Baloch, E. Zacharaki, Y. Fan, M. D. Schnall, and D. Shen, "STEP: spatiotemporal enhancement pattern for MR-based breast tumor diagnosis," *Medical Physics* **37**(7), pp. 3192–3204, 2009.

[9] S. Agner, S. Soman, E. Libfeld, M. McDonald, K. Thomas, S. Englander, M. A. Rosen, D. Chin, J. Nosher, and A. Madabhushi, "Textural kinetics: a novel dynamic contrast enhanced (DCE)-MRI feature for breast lesion classification," *Journal of Digital Imaging* **24**(3), pp. 446–463, 2011.

[10] M. Mahrooghy, A. B. Ashraf, D. Daye, C. Mies, M. Feldman, M. Rosen, and D. Kontos, "Heterogeneity wavelet kinetics from DCE-MRI for classifying gene expression based breast cancer recurrence risk," *Medical Image Computing and Computer-Assisted In-*

tervention (MICCAI) **LNCS 8150**(Part II), pp. 295–302, 2013.

[11] U. Castellani, M. Cristani, C. Combi, V. Murino, A. Sbarbati, and P. Marzola, "Visual MRI: Merging information visualization and non-parametric clustering techniques for mri dataset analysis," *Artificial Intelligence in Medicine* **44**(3), pp. 171–282, 2008.

[12] C. Lavinia, M. de Jongea, M. Van de Sandeb, P. Takb, A. J. Nederveena, and M. Maas, "Pixel-by-pixel analysis of DCE MRI curve patterns and an illustration of its application to the imaging of the musculoskeletal system," *Magnetic Resonance Imaging* **25**(5), pp. 604–612, 2007.

[13] M. J. Stoutjesdijk, J. Veltman, M. Huisman, N. Karssemeijer, J. Barents, and H. Huisman, "Automatic analysis of contrast enhancent in breast mri lesions using mean shift clustering for roi selection," *Journal of Magnetic Resonance Imaging* **26**(3), pp. 606–614, 2007.

[14] E. Eyal and H. Degani, "Model-based and model-free parametric analysis of breast dynamic-contrast-enhanced MRI," *NMR in Biomedicine* **22**(1), pp. 40–53, 2009.

[15] J. E. Levman and P. M. A. L. Warner, E. Causer, "A vector machine formulation with application to the computer-aided diagnosis of breast cancer from DCE-MRI screeening examinations," *Journal of Digital Imaging* **27**(1), pp. 145–151, 2014.

[16] M. Rakoczy, D. McGaughey, M. J. Korenberg, J. Levman, and A. L. Martel, "Feature selection in computer-aided breast cancer diagnosis via dynamic contrast-enhanced magnetic resonance images," *Journal of Digital Imaging* **26**(2), pp. 198–208, 2013.

[17] H. Hawighorst, M. Libicher, M. V. Knopp, T. Moehler, G. W. Kaufmann, and G. v. Kaick, "Evaluation of angiogenesis and perfusion of bone marrow lesions: role of semiquantitative and quantitative dynamic MRI," *Journal of Magnetic Resonance Imaging* **10**(3), pp. 286–294, 1999.

[18] C. S. P. van Rijswijk, M. J. A. Geirnaerdt, A. H. M. Taminiau, F. van Coevorden, A. H. Zwinderman, T. Pope, and J. L. Bloem, "Soft-tissue tumours: value of static and dynamic gadopentate dimeglumine-enhanced MR imaging in prediction of malignancy," *Radiology* **233**(2), pp. 493–502, 2004.

[19] K. L. Verstraete and P. Lang, "Bone and soft tissue tumors: the role of contrast agents for MR imaging," *European Journal of Radiology* **34**(3), pp. 229–246, 2000.

[20] J. Levman, T. Leung, P. Causer, D. Plewes, and A. L. Martel, "Classification of dynamic contast-enhanced magnetic resonance breast lesions by support vector mechines," *IEEE Transactions on Medical Imaging* **27**(5), pp. 688–696, 2008.

[21] J. Yao, "Breast tumor analysis in dynamic contrast enhanced MRI using texture features and wavelet transform," *IEEE Journal of Selected Topics in Signal Processing* **3**(1), pp. 94–100, 2009.

[22] C. Tanner, D. J. Hawkes, M. Khazen, P. Kessar, and M. O. Leach, "Does registration improve the performance of a computer aided diagnosis system for dynamic contrast-enhanced MR mammography?," *IEEE International Symposium on Biomedical Imaging* , pp. 466–469, 2006.

[23] S. Marrone, G. Piantadosi, R. Fusco, A. Petrillo, M. Sansone, and C. Sansone, "Automatic lesion detection in breast DCE-MRI," *The 17th International Conference on Image Analysis and Processing (ICIAP2013)* **LNCS8157**(Part II), pp. 359–368, 2013.

[24] M. Lustig, D. Donoho, and J. M. Pauly, "Sparse MRI: the application of compressed sensing for rapid MR imaging," *Magnetic Resonance Imaging* **58**(6), pp. 1182–1195, 2007.

[25] X. Yin, B. W. H. Ng, and D. Abbott, *Terahertz imaging for biomedical applications: pattern recognition and tomographic reconstruction*, Springer-Verlag, New York, USA, 2012.

[26] D. Martin and E. Puplett, "Polarised interferometric spectrometry for the millimetre and submillimetre spectrum," *Infrared Physics* **10**, pp. 105–109.

[27] D. M. Mittleman, R. Jacobsen, and M. Nuss, "T-Ray imaging," *IEEE Journal of Selected Topics in Quantum Electronics* **2**(679), pp. 679–692, 1996.

[28] D. Mittleman, R. Neelamani, R. B. J. Rudd, and M. Koch, "Recent advances in terahertz imaging," *Applied Physics B Lasers and Optics* **68**(6), pp. 1085–1094, 1999.

[29] R. M. Woodward, B. Cole, V. P. Walace, D. D. Arnone, R. Pye, E. H. Linfield, and M. Pepper, "Terahertz pulse imaging in reflection geometry of human skin cancer and skin tissue," *Journal of Investigative Dermatology* **47**(21), pp. 3853–3863, 2002.

[30] B. Ferguson, S. Wang, D. Gray, D. Abbott, and X. C. Zhang, "Identification of biological tissue using chirped probe THz imaging," *Microelectronics Journal* **33**(12), pp. 1043–1051, 2002.

[31] H. P. Siegel, "Terahertz technology in biology and medicine," *IEEE Transactions on Microwave Theory and Techniques* **52**(10), pp. 2438–2447, 2004.

[32] M. Brucherseifer, M. Nagel, P. H. Bolivar, H. Kurz, A. Bosserhoff, and R. Büttner, "Label-free probing of the binding state of DNA by time-domain terahertz sensing," *Applied Physics Letters* **77**(24), pp. 4049–4051, 2000.

[33] P. U. Jepsen, J. K. Jensen, and U. Møller, "Characterization of aqueous alcohol solutions in bottles with thz reflection spectroscopy," *Optics Express* **16**(13), pp. 9318–9331, 2008.

[34] A. G. Markelz, "Terahertz dielectric sensitivity to biomolecular structure and function," *Spectrochimica Acta, Part A: Molecular and Biomolecular Spectroscopy* **14**(1), pp. 180–190, 2008.

[35] A. Mazhorova, A. Markov, A. Ng, R. Chinnappan, O. Skorobogata, M. Zourob, and M. Skorobogatiy,

"Label-free bacteria detection using evanescent mode of a suspended core terahertz fiber," *Optics Express* **20**(5), pp. 5344–5355, 2012.

[36] T. Chen, Z. Li, and W. Mo, "Identification of biomolecules by terahertz spectroscopy and fuzzy pattern recognition," *Spectrochimica Acta, Part A: Molecular and Biomolecular Spectroscopy* **106**, pp. 48–53, 2013.

[37] A. Menikh, S. P. Mickan, H. Liu, R. MacColl, and X.-C. Zhang, "Label-free amplified bioaffinity detection using terahertz wave technology," *Biosensors and Bioelectronics* **20**(3), pp. 658–662, 2004.

[38] A. Menikh, R. MacColl, C. Mannella, and X. Zhang, "Terahertz biosensing technology: Frontiers and progress," *ChemPhysChem* **3**(8), pp. 655–658, 2002.

[39] B. Fischer, M. Hoffmann, H. Helm, R. Wilk, F. Rutz, T. Kleine-Ostmann, M. Koch, and P. Jepsen, "Terahertz time-domain spectroscopy and imaging of artificial RNA," *Optics Express* **13**(14), pp. 5205–5215, 2005.

[40] B. Fischer, M. Hoffmann, H. Helm, and P. U. Jepsen, "Chemical recognition in terahertz time-domain spectroscopy and imaging, semiconductor science and technology," *Semiconductor Science and Technology* **20**(7), pp. S246–S253, 2005.

[41] D. H. Martin and J. W. Bowen, "Long-wave optics," *IEEE Transactions on Microwave Theory and Techniques* **41**(10), pp. 1676–1690, 1993.

[42] S. Smye, J. Chamberlain, A. Fitzgerald, and E. Berry, "The interaction between terahertz radiation and biological tissue," *Physics in Medicine and Biology* **46**(9), pp. R101–R112, 2001.

[43] P. F. Taday, I. V. Bradley, D. D. Arnone, and M. Pepper, "Using terahertz pulse spectroscopy to study the crystalline structure of a drug: A case study of the polymorphs of ranitidine hydrochloride," *Journal of Pharmaceutical Sciences* **92**(4), pp. 831–838, 2003.

[44] S. Mickan, D. Abbott, J. Munch, X.-C. Zhang, and T. van Doornd, "Analysis of system trade-offs for terahertz imaging," *Microelectronics Journal* **31**(7), pp. 503–514, 2000.

[45] E. Pickwell and V. P. Wallace, "Biomedical applications of terahertz technology," *Journal of Physics D: Applied Physics* **39**(17), pp. R301–R310, 2006.

[46] O. Sushko, R. Dubrovka, and R. Donnan, "Sub-terahertz spectroscopy reveals that proteins influence the properties of water at greater distances than previously detected," *Journal of Chemical Physics* **142**(5), Art Number:055101, 2015.

[47] O. Sushko, R. Dubrovka, and R. Donnan, "Terahertz spectral domain computational analysis of hydration shell of proteins with increasingly complex tertiary structure," *Journal of Physical Chemistry B* **117**(51), pp. 16486–16492, 2013.

[48] S. R. K. C. Rønne, P. Åstrand, "THz spectroscopy of liquid H2O and D2O," *Physical Review Letters* **82**(14), pp. 2888–2891, 1999.

[49] S. Hadjiloucas, L. Karatzas, and J. W. Bowen, "Measurements of leaf water content using terahertz radiation," *IEEE Transactions on Microwave Theory and Techniques* **47**(2), pp. 142–149, 1999.

[50] S. Hadjiloucas and J. W. Bowen, "Precision of quasioptical null-balanced bridge techniques for transmission and reflection coefficient measurements," *Review of Scientific Instruments* **70**(1), pp. 213–219, 1999.

[51] R. M. Woodward, V. P. Wallace, R. J. Pye, B. E. Cole, D. Arnone, E. H. Linfield, and M. Pepper, "Terahertz pulse imaging of ex vivo basal cell carcinoma," *Journal of Investigative Dermatology* **120**(1), pp. 72–78, 2003.

[52] V. P. Wallace, A. J. Fitzgerald, S. Shankar, N. Flanagan, R. Pye, J. Cluff, and D. D. Arnone, "Terahertz pulsed imaging of basal cell carcinoma ex vivo and in vivo," *Journal of Investigative Dermatology* **151**(2), pp. 424–432, 2004.

[53] T. Lahtinen, J. Nuutinen, E. Alanen, M. Turunen, L. Nuortio, T. Usenius, and J. W. Hopewell, "Quantitative assessment of protein content in irradiated human skin," *International Journal of Radiation Oncology Biology Physics* **43**(3), pp. 635–638, 1999.

[54] M. K. Choi, K. Taylor, A. Bettermann, and D. W. van der Weide, "Broadband 10-300 GHz stimulus-response sensing for chemical and biological entities," *Physics in Medicine and Biology* **47**(21), pp. 3777–3789, 2002.

[55] A. G. Markelz, A. Roiberg, and E. J. Heilweil, "Pulsed terahertz spectroscopy of DNA, bovine serum albumin and collagen between 0.1 and 2.0 THz," *Chemical Physics Letters* **320**(1-2), pp. 42–48, 2000.

[56] P. Martel, P. Calmettes, and B. Hennion, "Vibrational modes of hemoglobin in red blood cells," *Biophysical Journal* **59**(2), pp. 363–377, 1991.

[57] P. Siegel, "Terahertz technology," *IEEE Transactions on Microwave Theory and Techniques* **50**(3), pp. 910–928, 2002.

[58] J. Nishizawa, T. Sasaki, K. Suto, T. Tanabe, K. Saito, T. Yamada, and T. Kimura, "THz transmittance measurements of nucleobases and related molecules in the 0.4- to 5.8-THz region using a GaP THz wave generator," *Optics Communications* **246**(1-3), pp. 229–239, 2005.

[59] M. Herrmann, H. Tabata, and T. Kawai, "Terahertz time-domain spectroscopy and imaging of DNA," in *International Quantum Electronics Conference*, pp. 1240–1241, 2005.

[60] M. Walther, B. Fischer, M. Schall, H. Helm, and P. U. Jepsen, "Far-infrared vibrational spectra of all-trans, 9-cis and 13-cis retinal measured by THz time-domain spectroscopy," *Chemical Physics Letters* **332**(3-4), pp. 389–395, 2000.

[61] I. Jones, T. J. Rainsford, B. Fischer, and D. Abbott, "Towards t-ray spectroscopy of retinal isomers: A review of methods and modelling," *Vibrational Spec-*

*troscopy* **41**(2), pp. 144–154, 2006.

[62] C. J. Strachan, P. F. Taday, D. Newnham, K. C. Gordon, J. A. Zeitler, M. Pepper, and T. Rades, "Using terahertz pulsed spectroscopy to study crystallinity of pharmaceutical materials," *Chemical Physics Letters* **390**(1-3), pp. 20–24, 2004.

[63] C. Strachan, P. Taday, D. Newnham, K. Gordon, J. Zeitler, M. Pepper, and T. Rades, "Using terahertz pulsed spectroscopy to quantify pharmaceutical polymorphism and crystallinity," *Journal of Pharmaceutical Sciences* **94**(4), pp. 837–846, 2005.

[64] C. J. Strachan, P. F. Taday, D. A. Newnham, K. C. Gordon, J. A. Zeitler, M. Pepper, and T. Rades, "Terahertz pulsed spectroscopy and imaging in the pharmaceutical setting - a review," *Journal of Pharmacy and Pharmacology* **59**(2), pp. 209–223, 2005.

[65] A. I. McIntosh, B. Yanga, S. M. Goldupb, M. Watkinsonb, and R. S. Donnana, "Crystallization of amorphous lactose at high humidity studied by terahertz time domain spectroscopy," *Chemical Physics Letters* **558**, pp. 104–108, 2013.

[66] S. Hadjiloucas, R. Galvão, J. Bowen, R. Martini, M. Brucherseifer, H. Pellemans, P. H. Bolivar, H. Kurz, J. Digby, G. Parkhurst, and J. Chamberlain, "Measurement of propagation constant in waveguides using wideband coherent thz spectroscopy," *Journal of the Optical Society of America B* **20**(2), pp. 391–401, 2003.

[67] R. Galvão, S. Hadjiloucas, V. Becerra, and J. Bowen, "Subspace system identification framework for the analysis of multimoded propagation of thz-transient signals," *Measurement Science and Technology* **16**(5), pp. 1037–1053, 2005.

[68] S. Qian, *Time-Frequency and Wavelet Transforms*, Prentice Hall, Inc., New Jersey, USA, 2002.

[69] T. Froese, S. Hadjiloucas, R. Galvão, V. Becerra, and C. Coelho, "Comparison of extrasystolic ecg signal classifiers using discrete wavelet transforms," *Pattern Recognition Letters* **27**(5), pp. 393–407, 2006.

[70] E. Berry, R. D. Boyle, A. J. Fitzgerald, and J. W. Handley, "Time frequency analysis in terahertz pulsed imaging," in *Computer Vision Beyond the Visible Spectrum (Advances in Pattern Recognition)*, B. Bhanu and I. Pavlidis, eds., pp. 290–329, Springer Verlag, London, UK, 2005.

[71] A. Meyer-Base, *Pattern Recognition for Medical Imaging*, Elsevier, California, USA, 2003.

[72] S. Hadjiloucas, R. Galvão, and J. Bowen, "Analysis of spectroscopic measurements of leaf water content at thz frequencies using linear transforms," *Journal of the Optical Society of America A* **19**(12), pp. 2495–2509, 2002.

[73] R. Galvão, S. Hadjiloucas, J. Bowen, and C. Coelho, "Optimal discrimination and classification of THz spectra in the wavelet domain," *Optics Express* **11**(12), pp. 1462–1473, 2003.

[74] J. W. Handley, A. Fitzgerald, E. Berry, and R. Boyle, "Wavelet compression in medical terahertz pulsed imaging," *Physics in Medicine and Biology* **47**(21), pp. 3885–3892, 2002.

[75] R. K. H. Galvão, S. Hadjiloucas, K. H. Kienitz, H. Paiva, and R. Afonso, "Fractional order modeling of large three-dimensional RC networks," *IEEE Transactions on Circuits and Systems I* **60**(3), pp. 624–637, 2013.

[76] R. K. H. Galvão, K. H. Kienitz, S. Hadjiloucas, G. Walker, J. Bowen, S. F. C. Soares, and M. C. U. Araújo, "Multivariate analysis of random three-dimensional RC networks in the time and frequency domains," *IEEE Transactions on Dielectrics and Electrical Insulation* **20**(3), pp. 995–1008, 2013.

[77] L. A. Jacyntho, M. C. M. Teixeira, E. Assunção, R. Cardim, R. K. H. Galvão, and S. Hadjiloucas, "Identification of fractional-order transfer functions using a step excitation," *IEEE Transactions on Circuits and Systems II, Express Briefs* , p. In Press, 2015.

[78] S. Hadjiloucas and J. Bowen, "Precision of quasi-optical null-balanced bridge techniques for transmission and reflection coefficient measurements," *Review of Scientific Instruments* **70**, pp. 213–219, 1999.

[79] R. Donnan and B. Yang, "Enhanced rapid and accurate sub-THz magneto-optical characterization of hexaferrite ceramics," *Journal of Magnetism and Magnetic Materials* **323**(15), pp. 1992–1997, 2011.

[80] B. Yang, R. Wylde, D. Martin, P. Goy, R. Donnan, and S. Caroopen, "The determination of the gyrotropic characteristics of hexaferrite ceramics from 75 to 600 GHz using an ultra-wideband vector-network-analyser," *IEEE Transactions on Microwave Theory and Techniques* **58**(12), pp. 3587–3597, 2010.

[81] W. Sun, B. Yang, X. Wang, Y. Zhang, and R. Donnan, "Accurate determination of terahertz optical constants by vector network analyzer of fabry-perot response," *Optics Letters* **38**(24), pp. 5438–5441, 2013.

[82] B. Ferguson, S. Wang, H. Zhong, D. Abbott, and X.-C. Zhang, "Powder retection with T-ray imaging," *Proceeding of SPIE Terahertz for Military and Security Applications* **5070**, pp. 7–16, 2003.

[83] M. Naftaly, *Terahertz Metrology*, Artech House, Boston London, 2015.

[84] M. Herrmann, M. Tani, and K. Sakai, "Display modes in time-resolved terahertz imaging," *Japanese Journal of Applied Physics Part 1-Regular Papers Short Notes & Review Papers* **39**(11), pp. 6254–6258, 2000.

[85] S. Bow, *Pattern Recognition and Image Preprocessing (Signal Processing and Communications Series)*, Marcel Dekker, Inc., NY, USA, 2002.

[86] C. Hayes, A. Padhani, and M. Leach, "Assessing changes in tumour vascular function using dynamic contrast enhanced magnetic resonance imaging," *NMR Biomedicine* **15**, pp. 154–163, 2002.

[87] A. Jackson, D. L. Buckley, G. J. M. Parker, and M. Ah-See, *Dynamic Contrast-Enhanced Magnet-*

ic Resonance Imaging in Oncology, Springer-Verlag, Heidelberg, Germany, 2005.

[88] P. D. Friedman, S. V. Swaminathan, and R. Smith, "SENSE imaging of the breast," *American Journal of Roentgenology* **184**(2), pp. 448–451, 2005.

[89] S. Ljunggren, "A simple graphical representation of fourier-based imaging methods," *Journal of Magnetic Resonance* **54**(2), pp. 338–343, 1983.

[90] D. Twieg, "The k-trajectory formulation of the N-MR imaging process with applications in analysis and synthesis of imaging methods," *Medical Physics* **10**(5), pp. 610–621, 1983.

[91] T. Parrish and X. Hu, "Continuous update with random encoding (CURE): a new strategy for dynamic imaging," *Magnetic Resonance in Medicine* **33**(3), pp. 326–336, 1995.

[92] R. C. Semelka, N. L. Kelekis, D. Thomasson, M. A. Brown, and G. A. Laub, "HASTE MR imaging: description of technique and preliminary results in the abdomen," *Journal of Magnetic Resonance Imaging* **6**(4), pp. 698–699, 1996.

[93] D. S. Smith, E. B. Welch, X. Li, L. R. Arlinghaus, M. E. Loveless, T. Koyama, J. C. Gore, and T. E. Yankeelov, "Quantitative effects of using compressed sensing in dynamic contrast enhanced MRI," *Physics in Medicine and Biology* **56**(15), pp. 4933–4946, 2011.

[94] H. Wang, Y. Miao, K. Zhou, Y. Yu, S. Bao, Q. He, Y. Dai, S. Xuan, B. Tarabishy, Y. Ye, and J. Hu, "Feasibility of high temporal resolution breast DCE-MRI using compressed sensing theory," *Medical Physics* **37**(9), pp. 4971–4981, 2010.

[95] L. Chen, M. C. Schabel, and E. V. R. DiBella, "Reconstruction of dynamic contrast enhanced magnetic resonance imaging of the breast with temporal constraints," *Magnetic Resonance Imaging* **28**(5), pp. 637–645, 2010.

[96] X. X. Yin, B. W. H. Ng, K. Ramamohanarao, A. Baghai-Wadji, and D. Abbott, "Exploiting sparsity and low-rank structure for the recovery of multi-slice breast MRIs with reduced sampling error," *Medical & Biological Engineering & Computing* **50**(9), pp. 991–1000, 2012.

[97] J. F. Cai, E. J. Candès, and Z. Shen, "A singular value thresholding algorithm for matrix completion," *SIAM Journal on Optimization* **20**(4), pp. 1956–1982, 2010.

[98] X.-C. Zhang, "Terahertz wave imaging: horizons and hurdles," *Physics in Medicine and Biology* **47**(21), pp. 3667–3677, 2002.

[99] X. Yin, B. W. H. Ng, D. Abbott, B. Ferguson, and S. Hadjiloucas, "Application of auto regressive models of wavelet sub-bands for classifying terahertz pulse measurements," *Journal of Biological Systems* **15**(4), pp. 551–571, 2007.

[100] D. Woolard, R. Kaul, R. Suenram, W. A. Hight, T. Globus, and A. Samuels, "Application of auto regressive models of wavelet sub-bands for classifying terahertz pulse measurements," *IEEE MTT-S International Microwave Symposium Digest* **15**(4), pp. 925–928, 1999.

[101] A. J. Fitzgerald, S. Pinder, A. D. Purushotham, P. O'Kelly, P. C. Ashworth, and V. P. Wallace, "Classification of terahertz-pulsed imaging data from excised breast tissue," *Journal of Biomedical Optics* **17**(1), Art. No. 016005, 2012.

[102] A. J. Fitzgerald, V. P. Wallace, M. Jimenez-Linan, L. Bobrow, R. J. Pye, A. D. Purushotham, and D. D. Arnone, "Terahertz pulsed imaging of human breast tumors," *Radiology* **239**(2), pp. 533–540, 2006.

[103] E. Pickwell, B. E. Cole, A. J. Fitzgerald, V. P. Wallace, and M. Pepper, "Simulation of terahertz pulse propagation in biological systems," *Applied Physics Letters* **84**(12), pp. 2190–2192, 2004.

[104] C. Yu, S. Fan, Y. Sun, and E. Pickwell-MacPherson, "The potential of terahertz imaging for cancer diagnosis: A review of investigations to date," *Quant Imaging Med Surg* **2**(1), pp. 33–45, 2012.

[105] G.-B. Huang, Q.-Y. Zhu, and C.-K. Siew, "Extreme learning machine: Theory and applications," *Neurocomputing* **70**(1-3), pp. 489–501, 2006.

[106] J. O'Connor, P. Tofts, K. Miles, L. Parkes, G. Thompson, and A. Jackson, "Dynamic contrast-enhanced imaging techniques: CT and MRI," *The British Journal of Radiology* **84**(2), pp. S112–S120, 2011.

[107] J. Shawe-Taylor and N. Cristianini, *Kernel Methods for Pattern Analysis*, Cambridge University Press, Cambridge, UK, 2004.

[108] R. Galvão, S. Hadjiloucas, A. Zafiropoulos, G. Walker, J. Bowen, and R. Dudley, "Optimization of apodization functions in thz transient spectrometry," *Optics Letters* **32**(20), pp. 3008–3010, 2007.

[109] S. G. Mallat, *A Wavelet Tour of Signal Processing*, San Diego: Academic Press, CA, 1999.

[110] I. Daubechies, *Ten lectures on wavelets*, Society for Industrial and Applied Mathematics, Philadelphia, USA, 1992.

[111] A. Jensen and A. La Cour-Harbo, *Ripples in Mathematics: The Discrete Wavelet Transform*, Springer Verlag, Berlin, Germany, 2001.

[112] S. Hadjiloucas, R. Galvão, V. Becerra, J. Bowen, R. Martini, M. Brucherseifer, H. Pellemans, P. Bolí, H. Kurz, and J. Chamberlain, "Comparison of state space and ARX models of a waveguide's THz transient response after optimal wavelet filtering," *IEEE Transactions on Microwave Theory and Techniques MTT* **52**(10), pp. 2409–2419, 2004.

[113] B. Ferguson and D. Abbott, "Denoising techniques for terahertz responses of biological samples," *Microelectronics Journal* **32**(12), pp. 943–953, 2001.

[114] Y. Kim, "Wavelet power spectrum estimation for high-resolution terahertz time-domain spectroscopy," *Journal of the Optical Society of Korea* **15**(1), pp. 103–108, 2011.

[115] P. Moulin, "Wavelet thresholding techniques for power spectrum estimation," *IEEE Transaction on Signal*

*Processing* **42**(11), pp. 126–136, 1994.

[116] H. Stephani, J. Jonuscheit, C. Robine, and B. Heise, "Automatically detecting peaks in terahertz time-domain spectroscopy," *The 20th International Conference on Pattern Recognition* , pp. 4468–4471, 2010.

[117] M. Otsuka, J. Nishizawa, J. Shibata, and M. Ito, "Quantitative evaluation of mefenamic acid polymorphs by terahertz-chemometrics," *Journal of Pharmaceutical Sciences* **99**(9), pp. 4048–4053, 2010.

[118] H. Wu, E. J. Heilweil, A. S. Hussain, and M. A. Khan, "Process analytical technology (pat): Quantification approaches in terahertz spectroscopy for pharmaceutical application," *Journal of Pharmaceutical Sciences* **97**(2), pp. 970–984, 2008.

[119] D. Zimdars, J. A. Valdmanis, J. S. White, G. Stuk, S. Williamson, W. P. Winfree, and E. I. Madaras, "Technology and applications of terahertz imaging non-destructive examination: Inspection of space shuttle sprayed on foam insulation," *AIP Conference Proceedings* **760**(1), pp. 570–577, 2005.

[120] R. P. Cogdill, R. N. Forcht, Y. C. Shen, P. F. Taday, J. R. Creekmore, C. A. Anderson, and J. K. Drennen III, "Comparison of terahertz pulse imaging and near-infrared spectroscopy for rapid, non-destructive analysis of tablet coating thickness and uniformity," *Journal of Pharmaceutical Innovation* **2**(1-2), pp. 29–36, 2007.

[121] J. Stolarek, "Improving energy compaction of a wavelet transform using genetic algorithm and fast neural network," *Archives of Control Sciences* **20**(4), pp. 417–433, 2010.

[122] Z. Wang, "Fast algorithms for the discrete W transform and for the discrete fourier transform," *IEEE Transactions on Acoustics, Speech, Signal Processing* **ASSP-32**, pp. 803–816, 1984.

[123] B. G. Lee, "A new algorithm for computing the discrete cosine transform," *IEEE Transactions on Acoustics, Speech, Signal Processing* **ASSP-32**, pp. 1243–1245, 1984.

[124] Y. Arai, T. Agui, and M. Nakajima, "A fast DCT-SQ scheme for images," *IEICE Transactions* **E-71**(11), pp. 1095–1097, 1988.

[125] E. Feig and S. Winograd, "Fast algorithms for the discrete cosine transform," *IEEE Transactions on Signal Processing* **40**(9), pp. 2174–2193, 1992.

[126] K. Wahid, V. Dimitrov, G. Jullien, and W. Badawy, "Error-free computation of daubechies wavelets for image compression applications," *Electronics Letters* **39**(5), pp. 428–429, 2003.

[127] A. Madanayake, R. J. Cintra, V. Dimitrov, F. M. Bayer, K. A. Wahid, S. Kulasekera, A. Edirisuriya, U. S. Potluri, S. K. Madishetty, and N. Rajapaksha, "Low-power VLSI architectures for DCT/DWT: Precision vs approximation for HD video, biomedical, and smart antenna applications," *IEEE Circuits and Systems Magazine* **15**(1), pp. 25–47, 2015.

[128] E. Morris and L. Liberman, *Pattern Classification and Scene Analysis*, John Wiley and Sons Inc, New York, NY, 1973.

[129] X. Yin, B. W. H. Ng, B. M. Fischer, B. Ferguson, and D. Abbott, "Support vector machine applications in terahertz pulsed signals feature sets," *IEEE Sensors Journal* **7**(12), pp. 1597–1608, 2007.

[130] L. Zhang, H. Zhong, D.-C. Zhu, J. Zuo, and C. Zhang, "Feature extraction without phase error for THz reflective spectroscopy," *Archives of Control Sciences* **55**(1), pp. 127–132, 2011.

[131] R. Tyniec, P. Zagrajek, and N. Palka, "Terahertz frequency domain spectroscopy identification system based on decision trees," *Acta Physica Polonica A* **122**(5), pp. 891–895, 2012.

[132] H. Stephani, B. Heise, K. Wiesauer, S. Katzletz, D. Molter, J. Jonuscheid, and R. Beigang, "A feature set for enhanced automatic segmentation of hyperspectral terahertz images," *Proceedings of the 2011 Irish Machine Vision and Image Processing Conference* , pp. 117–122, 2011.

[133] Q. Fu, L. M. Cheng, and F. Liu, "Terahertz time-domain spectroscopy analysis with wave atoms transform," *Proceedings of the 2011 Asia-Pacific Signal and Information Processing Association* **2013**(1), Art. No. APSIPA137, 2011.

[134] Z. Xu, J. Tu, J. Li, and Y. Pi, "Research on micro-feature extraction algorithm of target based on terahertz radar," *EURASIP Journal on Wireless Communications and Networking* **2013**(77), pp. 1–9, 2013.

[135] J. Schürmann, *Pattern Classification: A Unified View of Statistical and Neural Approaches*, John Wiley and Sons, Inc., New York, USA, 1996.

[136] R. Pan, S. Zhao, and J. Shen, "Terahertz spectra applications in identification of illicit drugs using support vector machines," *2010 Symposium on Security Detection and Information Processing* **7**, pp. 15–21, 2010.

[137] X. X. Yin, S. Hadjiloucas, J. He, Y. Zhang, Y. Wang, and D. Zhang, "Application of complex extreme learning machine to multiclass classification problems with high dimensionality: a THz spectra classification problem," *Digital Signal Processing* **108**(2), pp. 629–643, 2012.

[138] G. B. Huang, H. Zhou, X. Ding, and R. Zhang, "Extreme learning machine for regression and multiclass classification," *IEEE Transactions on Systems, Man, and Cybernetics, Part B: Cybernetics* **42**(2), pp. 513–529, 2011.

[139] G.-B. Huang, D. Wang, and Y. Lan, "Extreme learning machines: a survey," *International Journal of Machine Learning and Cybernetics* **2**(2), pp. 107–122, 2011.

[140] C. J. C. Burges, "A tutorial on support vector machines for pattern recognition," *Data Mining and Knowledge Discovery* **2**, pp. 121–167, 1998.

[141] V. Vapnik, *The Nature of Statistical Learning Theory*, Springer-Verlag, New York, USA, 1995.

[142] P. Bouboulis, K. Slavakis, and S. Theodoridis, "Adaptive learning in complex reproducing kernel hilbert spaces employing wirtinger's subgradients," *IEEE Transactions on Neural Networks and Learning Systems* **2**(99), pp. 260–276, 2012.

[143] F. A. Tobar, A. Kuh, and D. P. Mandic, "A novel augmented complex valued kernel LMS," in *the 7th IEEE Sensor Array and Multichannel Workshop 2012*, pp. 473–476, 2012.

[144] A. El-Gindy and G. M. Hadad, "Nonparametric bayes error estimation using unclassified samples," *Journal of AOAC International* **95**(3), pp. 609–623, 2012.

[145] M. E. Van-Valkenburg, "In memoriam: Hendrik W. Bode (1905-1982)," *IEEE Transactions on Automatic Control* **AC-29**(3), pp. 193–194, 1984.

[146] X. Yin, S. Hadjiloucas, and Y. Zhang, "Complex extreme learning machine applications in terahertz pulsed signals feature sets," *Computer methods and programs in biomedicine* **117**(2), pp. 387–403, 2014.

[147] L. Eadie, C. B. Reid, A. Fitzgerald, and V. Wallace, "Optimizing multi-dimensional terahertz imaging analysis for colon cancer diagnosis," *Expert Systems with Applications* **40**(6), pp. 2043–2050, 2013.

[148] J. Jensen, *Introductory Digital Image Processing–A Remote Sensing Perspective*, Prentice Hall, Inc., Upper Saddle River, New Jersey, 1996.

[149] M. A. Brun, F. Formanek, A. Yasuda, M. Sekine, N. Ando, and Y. Eishii, "Terahertz imaging applied to cancer diagnosis," *Physics in Medicine and Biology* **55**(16), pp. 4615–4623, 2010.

[150] M. W. Ayech and D. Ziou, "Terahertz image segmentation based on k-harmonic-means clustering and statistical feature extraction modeling," *21st IEEE International Conference on Pattern Recognition* , pp. 222–225, 2012.

[151] M. W. Ayech and D. Ziou, "Segmentation of terahertz imaging using k-means clustering based on ranked set sampling," *Expert Systems with Applications* **42**(6), pp. 2959–2974, 2015.

[152] M. W. Ayech and D. Ziou, "Automated feature weighting and random pixel sampling in k-means clustering for terahertz image segmentation," *IEEE Computer Vision and Pattern Recognition* , pp. 35–40, 2015.

[153] E. Leiss-Holzinger, K. Wiesauer, H. Stephani, B. Heise, D. Stifter, B. Kriechbaumer, S. J. Spachinger, C. Gusenbauer, and G. Withalm, "Imaging of the inner structure of cave bear teeth by novel non-destructive techniques," *Palaeontologia electronica* **18**(1), p. Art No. 18.1.1T, 2015.

[154] M. Brito, E. Chavez, A. Quiroz, and J. Yukich, "Connectivity of the mutual k-nearest-neighbor graph in clustering and outlier detection," *Probability Letter* **35**, pp. 33–42, 1997.

[155] E. Berry, J. W. Handley, A. J. Fitzgerald, W. J. Merchant, R. D. Boyle, N. N. Zinov'ev, R. E. Miles, J. M. Chamberlain, and M. A. Smith, "Multispectral classification techniques for terahertz pulsed imaging: an example in histopathology," *Medical Engineering & Physics* **26**(5), pp. 423–430, 2004.

[156] S. Orel, M. D. Schnall, C. M. Powell, M. G. Hochman, L. J. Solin, B. L. Fowble, M. H. Torosian, and E. F. Rosato, "Staging of suspected breast-cancer-effect of MR imaging and MR-guided imaging and biopsy," *Radiology* **196**(1), pp. 115–122, 1995.

[157] D. Saslow, C. Boetes, W. Burke, S. Harms, M. O. Leach, C. D. Lehman, E. Morris, E. Pisano, M. Schnall, S. Sener, R. A. Smith, E. Warner, M. Yaffe, K. S. Andrews, and C. A. Russell, "American cancer society guidelines for breast screening with MRI as an adjunct to mammography," *CA: A Cancer Journal for Clinicians* **57**(2), pp. 75–89, 2007.

[158] B. Szabó, P. Aspelin, M. Wiberg, and B. Bone, "Dynamic MR imaging of the breast - analysis of kinetic and morphologic diagnostic criteria," *Acta Radiologica* **44**(4), pp. 379–386, 2003.

[159] C. W. Piccoli, "Contrast-enhanced breast MRI: factors affecting sensitivity and specificity," *European Radiology* **7**(Suppl. 5), pp. S281–S288, 1997.

[160] K. Nie, J.-H. Chen, H. J. Yu, Y. Chu, O. Nalcioglu, and M.-Y. Su, "Quantitative analysis of lesion morphology and texture features for diagnostic prediction in breast MRI," *Acta Radiologica* **15**(12), pp. 1513–1525, 2008.

[161] B. K. Szabó, P. Aspelin, and M. K. Wiberg, "Neural network approach to the segmentation and classification of dynamic magnetic resonance images of the breast: comparison with empiric and quantitative kinetic parameters," *Acta Radiologica* **11**(12), pp. 1344–1354, 2004.

[162] T. Twellmann, A. Meyer-Baese, O. Lange, S. Foo, and T. W. Nattkemper

[163] W. Chen, M. L. Giger, U. Bick, and G. M. Newstead, "Automatic identification and classification of characteristic kinetic curves of breast lesion on DCE-MRI," *Acta Radiologica* **33**(8), pp. 2878–2887, 2006.

[164] C. E. McLaren, W.-P. Chen, K. Nie, and M.-Y. Su, "Prediction of malignant breast lesions from mri features: a comparison of artificial neural network and logistic regression techniques," *Acta Radiologica* **16**(7), pp. 842–851, 2009.

[165] L. A. Meinel, A. H. Stolpen, K. S. Berbaum, L. L. Fajardo, and J. M. Reinhardt, "Breast MRI lesion classification: improved performance of human readers with a backpropagation neural network computer-aided (CAD) system," *Journal of Magnetic Resonance Imaging* **25**(1), pp. 89–95, 2007.

[166] A. Penn, S. Thompson, R. Brem, C. Lehman, P. Weatherall, M. Schnall, G. Newstead, E. Conant, S. Ascher, E. Morris, and E. Pisano, "Morphologic blooming in breast MRI as a characterization of margin for discriminating benign from malignant lesions," *Acta Radiologica* **13**(11), pp. 1344–1354, 2006.

[167] P. Gibbs and L. W. Turnbull, "Texture analysis of

contast-enhanced MR images of the breast," *Magnetic Resonance in Medicine* **50**(1), pp. 92–98, 2003.

[168] H. Degani, V. Gusis, D. Weinstein, S. Fields, and S. Strano, "Mapping pathophysiological features of breast tumors by MRI at high spatial resolution," *Nature Medicine* **3**(7), pp. 780–782, 1997.

[169] D. Weinstein, S. Strano, P. Cohen, S. Fields, J. M. Gomori, and H. Degani, "Breast fibroadenoma: mapping of pathophysiologic features with three-time-point, contrast-enhanced MR imagingŮpilot study," *Radiology* **210**(1), pp. 233–240, 1999.

[170] E. A. M. Hauth, H. Jaeger, S. Maderwald, A. Muhler, R. Kimmig, and M. Forsting, "Quantitative 2- and 3-dimensional analysis of pharmacokinetic model-derived variables for breast lesions in dynamic, contrast-enhanced MR mammography," *European Journal of Radiology* **66**(6), pp. 300–308, 2008.

[171] J. Pan, B. E. Dogan, S. Carkaci, L. Santiago, E. Arribas, S. B. Cantor, and G. J. Whitman, "Comparing performance of the CADstream and thedynaCAD breast MRI CAD systems," *Journal of Digital Imaging* **26**(5), pp. 971–976, 2013.

[172] F. Keyvanfard, M. A. Shoorehdeli, M. Teshnehlab, K. Nie, and M.-Y. Su, "Feasibility of high temporal resolution breast DCE-MRI using compressed sensing theory," *Neural Computing and Applications* **22**(1), pp. 35–45, 2013.

[173] T. Helbich, "Contrast-enhanced magnetic resonance imaging of the breast," *European Journal of Radiology* **34**(3), pp. 208–219, 2000.

[174] F. Davnall, C. S. P. Yip, G. Ljungqvist, M. Selmi, F. Ng, B. Sanghera, B. Ganeshan, K. A. Miles, G. J. Cook, and V. Goh, "Assessment of tumor heterogeneity: an emerging imaging tool for clinical practice?," *Insights Imaging* **3**(6), pp. 573–589, 2012.

[175] C. E. Beckman and S. M. Smith, "Tensorial extensions of independent component analysis for multi-subject FMRI analysis," *NeuroImage* **25**(1), pp. 294–311, 2005.

[176] E. Hodneland, A. Lundervold, R. J., and A. Munthe-Kaas, "Normalized gradient fields for nonlinear motion correction of DCE-MRI time series," *Computerized Medical Imaging and Graphics* **38**(3), pp. 202–210, 2014.

[177] N. Michoux, J. P. Vallée, A. Pechère-Bertschi, X. Montet, L. Buehler, and B. E. Van Beers, "Analysis of contrast-enhanced MR images to assess renal function," *Magma* **19**(4), pp. 167–179, 2006.

[178] J. Tokuda, H. Mamata, R. R. Gill, N. Hata, R. Kikinis, R. F. Padera Jr, R. E. Lenkinski, D. J. Sugarbaker, and H. Hatabu, "Impact of nonrigid motion correction technique on pixel-wise pharmacokinetic analysis of free-breathing pulmonary dynamic contrast-enhanced MR imaging," *Journal of Magnetic Resonance Imaging* **33**(4), pp. 968–973, 2011.

[179] J. P. B. O'Connor, A. Jackson, G. J. M. Parker, and G. C. Jayson, "DCE-MRI biomarkers in the clinical evaluation of antiangiogenic and vascular disrupting agents," *British Journal of Cancer* **96**, pp. 189–195, 2007.

[180] D. Zikic, S. Sourbron, X. X. Feng, H. J. Michaely, A. Khamene, and N. Navab, "Automatic alignment of renal DCE-MRI image series for improvement of quantitative tracer kinetic studies," *Proceedings of the SPIE* **6914**, Art. No. 691432, 2008.

[181] D. Rueckert, L. I. Sonoda, C. Hayes, D. L. G. Hill, M. O. Leach, and D. J. Hawkes, "Nonrigid registration using free-form deformations: Application to breast mr images," *IEEE Transactions on Medical Imaging* **18**(8), pp. 712–721, 1999.

[182] T. Rohlfing, C. R. Maurer, W. G. O'Dell, and J. Zhong, "Modeling liver motion and deformation during the respiratory cycle using intensity-based nonrigid registration of gated MR images," *Medical Physics* **31**(3), pp. 427–432, 2004.

[183] Y. Yim, H. Hong, and Y. G. Shin, "Deformable lung registration between exhale andinhale ct scans using active cells in a combined gradient force approach," *Medical Physics* **37**(8), pp. 4307–4017, 2010.

[184] G. Janssens, L. Jacques, J. O. de Xivry, X. Geets, and B. Macq, "Diffeomorphic registra-tion of images with variable contrast enhancement," *International Journal of Biomedical Imaging* **2011**(3), p. Art. No. 891585, 2011.

[185] T. Mansi, X. Pennec, M. Sermesant, H. Delingette, and N. Ayache, "Logdemons revisited: consistent regularisation and incompressibility constraint for soft tissue track-ing in medical images," *Medical Image Computing and Computer-Assisted Intervention - MICCAI 2010* **LNCS6362**, pp. 652–659, 2010.

[186] J. Modersitzki, "FLIRT with rigidity-image registration with a local non-rigidity penalty," *International Journal of Computer Vision* **76**(2), pp. 153–163, 2007.

[187] A. D. Merrem, F. G. Zöllner, M. Reich, A. Lundervold, J. Rorvik, and L. R. Schad, "A variational approach to image registration in dynamic contrast-enhanced MRI of the human kidney," *Magnetic Resonance Imaging* **31**(5), pp. 771–777, 2013.

[188] V. S. Lee, H. Rusinek, M. E. Noz, P. Lee, M. Raghavan, and E. L. Kramer, "Dynamic three dimensional MR renography for the measurement of single kidney function: initial experience," *Radiology* **227**(1), pp. 289–294, 2003.

[189] T. Song, V. L. Lee, H. Rusinek, M. Kaur, and A. F. Laine, "Automatic 4-D registration in dynamic MR renography based on over-complete dyadic wavelet and fourier transforms," *Proceedings of the 8th International Conference on Medical Image Computing and Computer-Assisted Intervention* **LNCS3750**(Part II), pp. 205–213, 2005.

[190] G. A. Buonaccorsi, J. P. O'Connor, A. Caunce, C. Roberts, S. Cheung, Y. Watson, K. Davies, L. Hope, A. Jackson, G. C. Jayson, and G. J. Parker,

"Tracer kinetic model-driven registration for dynamic contrast-enhanced MRI timeseries data," *Magnetic Resonance in Medicine* **58**(5), pp. 1010–1019, 2007.

[191] G. A. Buonaccorsi, C. Roberts, S. Cheung, Y. Watson, J. P. O'Connor, K. Davies, A. Jackson, G. C. Jayson, and G. J. Parker, "Comparison of the performance of tracer kinetic model-driven registration for dynamic contrast enhanced MRI using different models of contrast enhancement," *Academic Radiology* **13**(9), pp. 1112–1123, 2006.

[192] Y. Sun, J. Moura, and C. Ho, "Subpixel registration in renal perfusion MR image sequence," *Proceeding of IEEE International Symposium on Biomedical Imaging: Nano to Macro* **1**, pp. 700–703, 2004.

[193] F. G. Zöllner, R. Sance, P. Rogelj, M. J. Ledesma-Carbayo, J. Rørvik, A. Santos, and A. Lundervold, "Assessment of 3D DCE-MRI of the kidneys using non-rigid image registration and segmentation of voxel time courses," *Computerized Medical Imaging and Graphics* **33**(3), pp. 171–181, 2008.

[194] H. J. Johnson and G. E. Christensen, "Consistent landmark and intensity-based image registration," *IEEE Transactions on Medical Imaging* **21**(5), pp. 450–461, 2002.

[195] T. Rohlfing, C. R. Maurer Jr., D. A. Bluemke, and M. A. Jacobs, "Volume-preserving nonrigid registration of MR breast images using free-form deformation with an incompressibility constraint," *IEEE Transactions on Medical Imaging* **22**(6), pp. 730–741, 2003.

[196] D. Loeckx, F. Maes, D. Vandermeulen, and P. Suetens, "Nonrigid image registration using free-form deformations with a local rigidity constraint," *Medical Image Computing and Computer-Assisted Intervention - MICCAI 2004* **LNCS3216**, pp. 639–646, 2004.

[197] S. S., U. Preim, G. S., B. Preim, and T. K. D., "Local similarity measures for lesion registration in DCE-MRI of the breast," *Annals of the BMVA* **2011**(3), pp. 1–13, 2011.

[198] S. Glaßer, S. Schäfer, S. Oeltze, U. Preim, K. Tönnies, and B. Preim, "A visual analytics approach to diagnosis of breast DCE-MRI data," *Computers & Graphics* **34**(5), pp. 602–611, 2010.

[199] F. G. Zöllner, R. Sance, P. Rogelj, M. J. Ledesma-Carbayo, J. Rørvik, A. Santos, and A. Lundervold, "Assessment of 3D DCE-MRI of the kidneys using non-rigid image registration and segmentation of voxel time courses," *Computerized Medical Imaging and Graphics* **33**(1), pp. 171–181, 2009.

[200] M. Bhushan, J. A. Schnabel, L. Risser, M. P. Heinrich, J. M. Brady, and M. Jenkinson, "Motion correction and parameter estimation in DCE-MRI sequences: application to colorectal cancer," *Medical Image Computing and Computer-Assisted Intervention - MICCAI 2011* **LNCS6891**(Part I), pp. 476–483, 2011.

[201] W. Lin, J. Guo, M. A. Rosen, and H. K. Song, "Respiratory motion-compensated radial dynamic contrast-enhanced (dce)-mri of chest and abdominal lesions," *Magnetic Resonance in Medicine* **60**(5), pp. 1135–1146, 2008.

[202] J. B. Antoine Maintz and M. A. Viergever, "A survey of medical image registration," *Computing Surveys* **24**(4), pp. 325–376, 1992.

[203] A. N. Kumar, K. W. Short, and D. W. Piston, "A motion correction framework for time series sequences in microscopy images," *Microscopy and Microanalysis* **19**(2), pp. 433–450, 2013.

[204] L. Zhukov, K. Museth, D. Breen, R. Whitakery, and A. H. Barr, "Level set modeling and segmentation of DT-MRI brain data," *Journal of Electronic Imaging* **12**(1), pp. 125–133, 2003.

[205] T. F. Chan and L. A. Vese, "Active contours without edges," *IEEE Transactions on Image Processing* **10**(2), pp. 266–277, 2001.

[206] X. X. Yin, B. W.-H. Ng, Q. Yang, A. Pitman, K. Ramamohanarao, and D. Abbott, "Anatomical landmark localization in breast dynamic contrast-enhanced MR imaging," *Medical & Biological Engineering & Computing* **50**(1), pp. 91–101, 2012.

[207] X. X. Yin, B. W.-H. Ng, K. Ramamohanarao, and D. Abbott, "Tensor based sparse decomposition of 3D shape for visual detection of mirror symmetry," *Computer Methods and Programs in Biomedicine* **108**(2), pp. 629–643, 2012.

[208] M. A. O. Vasilescu and D. Terzopoulos, "Multilinear analysis of image ensembles: Tensorfaces," *Proceeding of the European Conference on Computer Vision* , pp. 447–460, 2002.

[209] T. Hazan, S. Polak, and A. Shashua, "Sparse image coding using a 3D non-negative tensor factorization," *Proceeding of the Tenth IEEE International Conference on Computer Vision* **1**, pp. 50–57, 2005.